Journal of
Marine Science and Engineering

MDPI

Article

CFD-FEM Simulation of Slamming Loads on Wedge Structure with Stiffeners Considering Hydroelasticity Effects

Zhenwei Chen [1], Jialong Jiao [1,2,*], Qiang Wang [3] and Shan Wang [4]

1 School of Civil Engineering and Transportation, South China University of Technology, Guangzhou 510641, China
2 State Key Laboratory of Coastal and Offshore Engineering, Dalian University of Technology, Dalian 116024, China
3 Department of Energy and Power Engineering, Shanxi Institute of Energy, Taiyuan 030600, China
4 Centre for Marine Technology and Ocean Engineering (CENTEC), Instituto Superior Técnico, Universidade de Lisboa, 1049-001 Lisbon, Portugal
* Correspondence: jiaojl@scut.edu.cn

Abstract: In this paper, both numerical and experimental methods are adopted to study the fluid–structure interaction (FSI) problem of a wedge structure with stiffeners impacted with water during the free-falling water entry process. In the numerical model, a partitioned two-way couple of CFD and FEM solvers is applied to deal with the FSI problem, where the external fluid pressure exported from the CFD simulation is used to derive the structural responses in the FEM solver, and the structural deformations are fed back into the CFD solver to deform the mesh. Moreover, a tank experiment using a steel wedge model that has the same structural properties is also conducted to compare with the numerical results. Verification and validation of the numerical results indicate that the CFD-FEM coupled method is feasible and reliable. The slamming response results by numerical simulation and experiments, including displacement, velocity, acceleration, slamming pressure, deformation, structural stresses and total forces on the wedge, accounting for hydroelasticity effects in different free falling height conditions are comprehensively analyzed and discussed.

Keywords: water entry; wedge structure; slamming loads; CFD-FEM coupled method; tank model experiment

check for updates

Citation: Chen, Z.; Jiao, J.; Wang, Q.; Wang, S. CFD-FEM Simulation of Slamming Loads on Wedge Structure with Stiffeners Considering Hydroelasticity Effects. *J. Mar. Sci. Eng.* **2022**, *10*, 1591. https://doi.org/10.3390/jmse10111591

Academic Editor: Md Jahir Rizvi

Received: 26 September 2022
Accepted: 25 October 2022
Published: 27 October 2022

Publisher's Note: MDPI stays neutral with regard to jurisdictional claims in published maps and institutional affiliations.

Copyright: © 2022 by the authors. Licensee MDPI, Basel, Switzerland. This article is an open access article distributed under the terms and conditions of the Creative Commons Attribution (CC BY) license (https://creativecommons.org/licenses/by/4.0/).

1. Introduction

The slamming phenomenon is one of the most concerning issues in the field of naval architecture and ocean engineering [1]. Slamming events occur when a structure is impacted with water at a relatively high speed, which is a strongly nonlinear problem involving fluid–structure interaction (FSI) issues in the presence of violent free surface flow and splash. When a ship sails in rough seas, the tremendous slamming loads caused by the ship's structure interacting with waves may result in local or global damage to the ship structure. Ship slamming can be investigated along with ship seakeeping and wave loads by both numerical and experimental methods [2,3]. However, due to the strong non-linearity and randomicity of ship slamming loads, it is more often investigated using a simplified hull structure, e.g., a wedge structure, entering into calm water, considering one or a partial degree-of-freedom (DOF) released.

The earliest research on slamming was carried out by the pioneering works of von Karman [4] and Wagner [5], investigating airplane ditching problems. In their work, water entry of a two-dimensional wedge and flat plate are addressed using empirical or analytical methods. Many analytical and numerical approaches were proposed based on their initial works [6]. For example, Cumberbatch [7] studied the impact of water of a wedge shape on a wall using a theoretical approach. Zhao and Faltinsen [8] presented a boundary element method for studying water entry of a two-dimensional body of arbitrary cross-section.

Faltinsen [9] studied water entry of a wedge with stiffened plates, considering hydroelasticity effects by solving the two-dimensional Laplace equation in the cross-sectional fluid domain by a generalized Wagner's theory. Watanabe [10] presented a general expression for the pressure distribution on inclined ship-like bodies penetrating a water surface by a matched asymptotic expansion.

However, due to the limitation of inviscid flow assumption, some complex flow physics and phenomena, such as flow separation, fluid splash, and viscous effects, cannot be well considered in the framework of potential flow theory or using analytical methods. On the other hand, Computational Fluid Dynamics (CFD) methods, which are suitable for simulating violent free surface flow and some strongly nonlinear issues such as instantaneous wetted surface and high-speed fluid structure impact effects, are becoming increasingly popular and mature [11]. In the past decades, CFD has been widely used to solve FSI problems and slamming issues. For example, Brizzolara et al. [12] compared the slamming pressure on a two-dimensional bow section obtained by different methods, including potential flow theory, explicit finite element code LS-DYNA, CFD-based FLOW-3D and FLUENT. Wang and Guedes Soares [13] predicted slamming loads on the stern of a chemical tanker by using an Arbitrary Lagrangian Eulerian (ALE) algorithm with LS-DYNA and compared with that of a Modified Longvinovich Model (MLM) with potential velocity theory. Xie et al. [14] studied the water entry problem of a bow-flare section with a bulbous bow by FLUENT software. Farsi and Ghadimi [15] simulated two-dimensional symmetry and asymmetry wedge water entry using the smoothed particle hydrodynamics (SPH) method. As an open source library CFD tool, OpenFOAM has also been widely used in the simulation of the water entry problem. For example, Wang et al. [16] studied the three-dimensional effects on slamming loads of wedges during water entry using OpenFOAM. Wang et al. [17] studied water entry of a symmetric/asymmetric wedge into waves using OpenFOAM. Bakica et al. [18] coupled the hydrodynamic solver OpenFOAM with the structural FE solver to solve hydro–structure interaction problems of ship wave loads and slamming loads, considering hydroelasticity.

Although CFD captures most complexities of the fluid physics with few assumptions, the structural response or stress cannot be solved by the CFD tool. Real ocean engineering structures are flexible rather than rigid. The structural strength and load responses are also concerning, in addition to external fluid pressure or loads. Hydroelastic effects should also be considered to predict the structural deformations and stresses if the structural elasticity is obvious. Yu et al. [19] conducted hydroelastic analysis on water entry of a constant velocity wedge with stiffened panels by combining a semi-analytical hydrodynamic impact theory with the mode superposition method for the structure. Luo et al. [20] developed an uncoupled method combining Wagner theory and the finite element method (FEM) to analyze the slamming problem for the three-dimensional structure. Xie et al. [21] combined the CFD and FEM solvers to provide the uncoupled solutions of hull structure water entry, where the hydrodynamic pressure was predicted by the Volume of Fluid (VOF) method, and the structural deflection was obtained by the quasi-static FEM analysis.

For the uncoupled method, only the fluid pressures acting on the structure are transferred to the structural solver, which is also called one-way coupling. For strong coupled FSI problems, two-way coupling should be considered, as the structural deformations are also fed back into the fluid solver and cause mesh deformations [22]. The CFD-FEM two-way coupled method has been used to study ship hydroelasticity and slamming issues. For example, Sun et al. [23] investigated the motion, structural response, and cavitation bubble evolution of a cylinder in the high-speed water entry process using STAR-CCM+ and Abaqus as a two-way coupling manner. Shi et al. [24] investigated the acceleration, pressure, stress and structural deformation of an elastic AUV during water entry impact using LS-DYNA software and tank experiment. Jiao et al. [25] adopted the CFD-FEM two-way coupled method to simulate wave-induced ship motions and loads and the slamming loads on a container ship. Liu et al. [26] developed a viscous flow hydro-elastoplastic approach by combining CFD and nonlinear FEM to predict ship wave loads and structural collapse. Yan et al. [27] used a partitioned two-way coupled CFD-FEA FSI method to study the water entry of flat plates with different impact velocities and wedges with different deadrise angles.

The scaled model test is essential for research of the water entry problem. Since the duration of the impact event is usually very short, high sampling rates such as 5–10 kHz are required for pressure measurement. This makes the slamming experiments more challenging compared with other common hydrodynamic load experiments. The experimental model usually has a constant water-entry speed via a motor or free falls under gravitational acceleration. Zhao et al. [28] conducted drop tests for a wedge with a deadrise angle of 30° and a bow flare section. De Backer et al. [29] performed drop tests on a hemisphere and two conical shapes with different deadrise angles and measured bottom slamming of these axisymmetric objects. Dong et al. [30] conducted drop tests using steel and aluminum wedges that have different structural elasticity to investigate the influence of structural elasticity on the impact force. Jiang et al. [31] investigated the air cushion effect on the slamming loads acting on a trimaran cross deck during water entry by both CFD and experiments. To summarize, the majority of the existing drop experiments focus on the impact pressure on the body surface while ignoring the structural elasticity or internal frame structures of the model.

In this paper, a partitioned CFD-FEM two-way coupled method is adopted to simulate the slamming and water entry problem of a wedge with stiffeners, considering hydroelasticity. A tank model experiment was also conducted, which proves that the CFD-FEM two-way coupled technique is feasible and reliable in simulating the water entry problem of flexible structures. Verification and validation of the numerical results were systematically conducted. Almost all the physical characteristics of interest within the scope of water impact and structural response can be satisfactorily reproduced by the presented CFD-FEA co-simulation approach, which include displacement, velocity, acceleration, slamming pressure, deformation, structural stresses and total forces on the wedge accounting for hydroelasticity effects, as well as graphical visualizations. Therefore, it is believed that this method has wide application values in slamming simulations, and it is a more powerful tool compared with analytical methods, potential flow theory or traditional CFD methods.

2. Model Description and Experimental Setup

2.1. Wedge Structure Description

In this study, a three-dimensional wedge steel structure with a deadrise angle of 45° is adopted as the research objective model. The mass of the wedge structure is 553 kg. As shown in Figure 1, the cross-section of the wedge has a dimension of 900 mm wide by 750 mm high. The longitudinal parallel length of the wedge is 1500 mm, which is large enough to ignore the difference in two-dimensional and three-dimensional effects caused by longitudinal flow during water entry. The shell, including the bottom plate and side plate, has a thickness of 5 mm.

To better reproduce the structural response of real ship structure, stiffeners are designed and mounted on the inner surface of the wedge. The stiffeners include a longitudinal bone and transverse frame. The T-profile longitudinal bone has a dimension of 50 × 35 × 5 mm, representing web height by wing width by thickness, respectively. Two longitudinal bones are arranged over the width of bottom plate, with a distance of 225 mm for both two sides. Four transverse frames, whose sectional parameter is 70 mm high by 5 mm thick, are equally arranged over the longitudinal span to act as the transverse bulkhead of real ship. The main parameters of the wedge structure and the stiffeners are listed in Table 1. Table 2 shows the coordinate position of fluid pressure monitoring point P1–5 and structural stress monitoring point S1–3, where the bottom point of wedge is set at the coordinate origin.

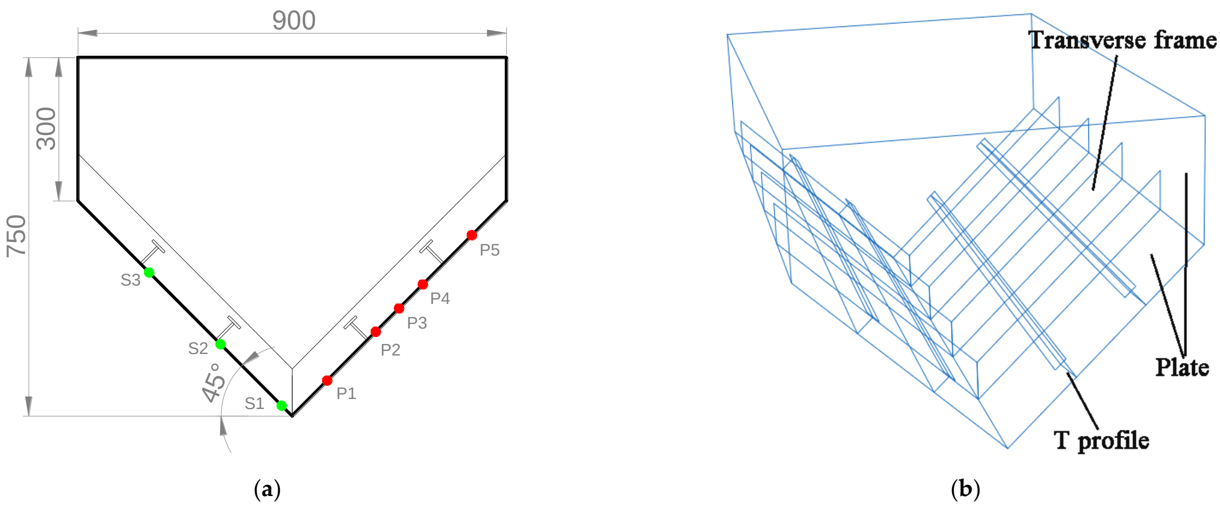

Figure 1. Sketch of the wedge structure model. (**a**) transverse plane (unit in mm); (**b**) 3D perspective view.

Table 1. Main parameters of the wedge structure and the stiffeners.

Content	Item	Parameter
Main dimension	Length (mm)	1500
	Width (mm)	900
	Height (mm)	750
	Deadrise angle (°)	45
	Mass (kg)	553
Component dimension	External plate thickness (mm)	5
	Longitudinal bone (mm)	$T\frac{5\times35}{5\times50}$
	Transverse frame (mm)	5×70
Material property	Density (kg/m^3)	7850
	Young's modulus (Gpa)	206
	Poisson ratio	0.3

Table 2. Coordinate position of measurement point.

Point	y (mm)	z (mm)
P1	74	74
P2	176	176
P3	225	225
P4	275	275
P5	378	378
S1	215	215
S2	150	150
S3	300	300

2.2. Experimental Setup

The model experiment was carried out at the ship model towing tank laboratory of Harbin Engineering University. The tank has a dimension of 108 m long by 7 m wide by 3.5 m deep. A dedicated mechanical device was designed to allow the free falling test of structures in the towing tank laboratory [30]. As shown in Figure 2a, the mechanical device is supported by a carriage rail that crosses the tank width. The mechanical device includes several parts, i.e., supporting steel frame, elevating installation, releasing installation and data acquisition system. Four vertical sliders are installed on the supporting steel frame to ensure the water entry direction of the wedge is exactly vertical in the downward direction.

The friction resistance of the slider and air resistance during free falling movement of the wedge are not considered.

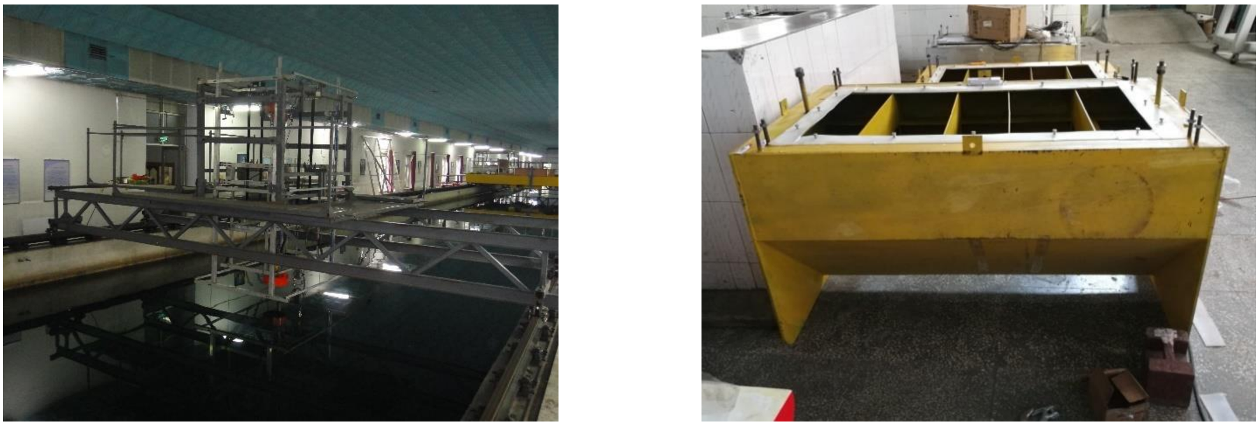

(**a**) (**b**)

Figure 2. Experimental model setup. (**a**) mechanical device for free-falling test; (**b**) wedge structure steel model.

As shown in Figure 2b, the wedge model was built by steel plate welding. It is noted that two flat baffles are installed at two longitudinal ends of the wedge to prevent the longitudinal flow effects during water entry. At the middle transverse section, five pressure sensors P1–5 are arranged on the wedge shell. The measuring range of the pressure sensor is a 100 m water column, and the accuracy is 0.1% full scale. The sampling frequency of the pressure is set at 10,000 Hz to ensure the slamming pressure peak can be well captured, as slamming is a transient phenomenon, and the peak lasts for a very short period, in the magnitude of millisecond, if the speed is high. A displacement sensor is installed at the top of the model to measure vertical drop distance. The measuring range of the displacement sensor is 3200 mm, and the accuracy is 0.1% full scale. The velocity of the model during the water entry process can be obtained by differentiating the displacement data.

2.3. Investigation Conditions

The model is released at four different heights to study the influence of initial water entry speed on slamming effects. The model is subject to free-falling motion under gravitational acceleration and then enters into and impacts with calm water. The involved conditions are listed in Table 3.

Table 3. Investigation conditions involved in this study.

Case ID	1	2	3	4
Falling height (m)	0.1	0.4	0.7	1.0
Initial speed when contact water (m/s)	1.400	2.800	3.704	4.427
Maximum speed during water entry process (m/s)	2.143	3.014	3.803	4.482

3. Numerical Model Setup

3.1. CFD-FEM Two-Way Coupled Approach

The numerical computations of the wedge structure's water entry process are performed by coupling the CFD solver STAR-CCM+ and the FEM solver Abaqus in a partitioned two-way coupling manner with the SIMULIA co-simulation engine. The basic algorithm and method of the two-way co-simulation are described as follows.

A framework of the partitioned two-way interaction between the CFD and FEM solvers is shown in Figure 3. The external surface of the wedge shell is defined as the data interaction surface between the CFD and FEM solvers. During each coupling time step, the fluid pressure and wall shear force calculated by the hydrodynamic solver are exported into the structure solver. The structure solver then feeds back the node displacement of the structure body to the hydrodynamic solver to update the fluid–structure coupling interface, where both overset mesh and morpher techniques are used in STAR-CCM+. The co-simulation will proceed to the next time step once the convergence condition is achieved. The convergence is achieved by satisfying any one of the following two criteria that comes first: (a) the convergence of the root mean square (RMS) residual values is below 1×10^{-4}; or (b) the maximum inner iteration times four is completed. In the present coupling method, surface-to-surface mapping in the coupling allows the exchange of data between the CFD model's boundaries and FE model's surfaces. The least square method is used to obtain the pressure at the structural node from the data of fluid loads. When the morphing displacement data is transferred from Abaqus to STAR-CCM+, the shape function method is adopted to interpolate the data from nodes to center points.

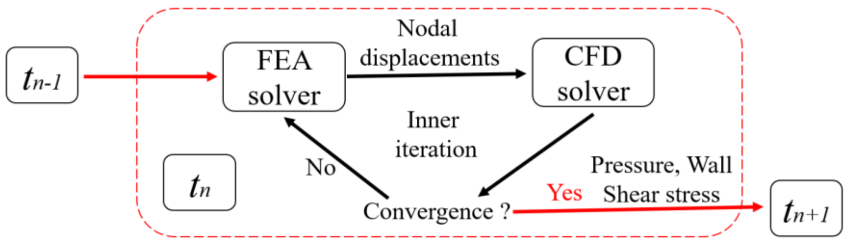

Figure 3. Procedure of two-way coupling during one time step.

With the occurrence of violent flow, such as flow separation and fluid splash during high speed water entry, slamming is a typical strongly nonlinear FSI problem, which implies that the structure and fluid interact strongly and that the time interval of the problem is relevant. The FSI exchange will therefore occur at regular intervals, and the information is tightly transferred between the CFD solver and the FEM solver. Therefore, an implicit coupling and iterative stagger is applied to solve the present slamming problem to ensure strong coupling and convergence during the information exchange between the two solvers in each coupling time step. Figure 4 demonstrates the calculation procedure of the parallel algorithm during implicit coupling simulation between partitioned multi-physics CFD and FEM solvers, where both CFD and FEM codes do the calculation simultaneously. Several iterations between the CFD and FEM solvers will take place during each coupling time step, Δt. The number of such iterations per time step is critical for the stability and accuracy of the coupled simulations.

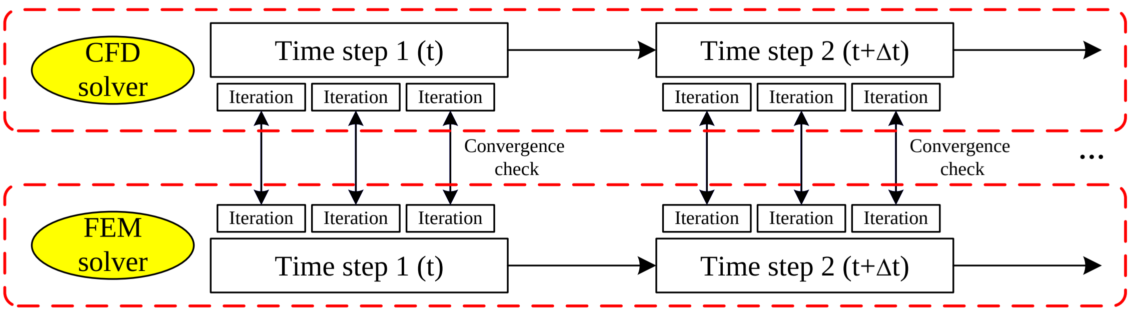

Figure 4. Framework of the implicit coupling procedure.

3.2. The CFD Model

The finite volume method (FVM)-based commercial software STAR-CCM+ is applied for the fluid flow solution. The unsteady, viscous, turbulent and incompressible flow around the wedge is governed by the continuity and Navier–Stokes equations. A second-order upwind scheme is used to discretize the convection term. A predictor-corrector approach is used to link the continuity and momentum equations. The Semi-Implicit Method for Pressure Linked Equations (SIMPLE) is employed to achieve an implicit coupling between pressure and velocity. The Realizable k-ε turbulence model is adopted to solve the continuity equation and momentum equation. The VOF method is used to simulate the free surface between the water and the air by solving an additional transport equation for an extra scalar variable known as the volume fraction. A High-Resolution Interface Capturing (HRIC) discretization scheme is used to track sharp interfaces between the two immiscible fluid components. Details of the basic governing equations of the CFD solver can be found in Refs. [32,33].

Figure 5 presents a general view of the computational model and fluid domain of the numerical tank. In the CFD model, only the wedge surface geometry information is used; the internal structure is not involved. The computational domain size of the numerical tank is 4.5 m long by 4.5 m wide by 4.5 m high. The height of water domain and air domain is 3.0 m and 1.5 m, respectively. The wedge model is located at the center of the tank. The origin of the coordinate system is located at the center of the horizontal plane and the calm water surface vertically. The x-axis, y-axis and z-axis coincide with the longitudinal, transverse and vertical direction of the wedge, respectively. The boundary condition of the no-slip wall is applied at the four side walls and the bottom of the numerical tank as well as the wedge surface, while the pressure outlet is applied at the top boundary condition.

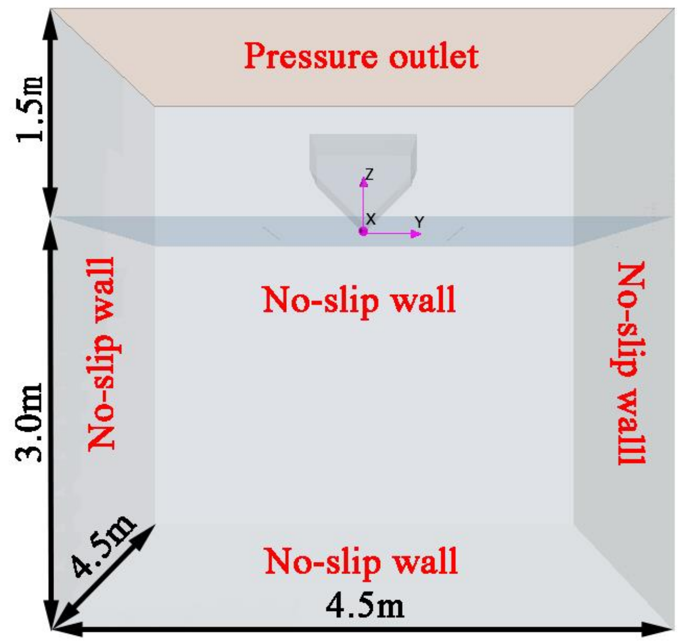

Figure 5. Numerical tank and boundary conditions.

As shown in Figure 6, the fluid domain includes a background region and an overset region. The overset region is defined around the wedge model to describe the rigid body motions, while the structural deformation of the wedge is realized by the morphing grid technique. The transmission of fluid flow data between the overset region and background region at each time step is realized based on the overset technique. Mesh generation was performed using the STAR-CCM+ built-in automated meshing toolbox. Unstructured hexahedral cells with trimmed cells adjacent to the wedge model are generated. The trimmed cells are identified as hexahedral cells. Local refinement of the grid is performed near the wedge model and the free surface. In the computational domain there are 3.01 million cells in total, among which 0.53 million cells are located in the overset region. The prism layer mesher generates orthogonal prismatic cells near the boundaries of walls with no-slip conditions. The thickness of the prism layer increases progressively, with a refinement ratio of 1.2. A boundary layer mesh of 5 cells near the wedge is selected (y + value lies in 30−60).

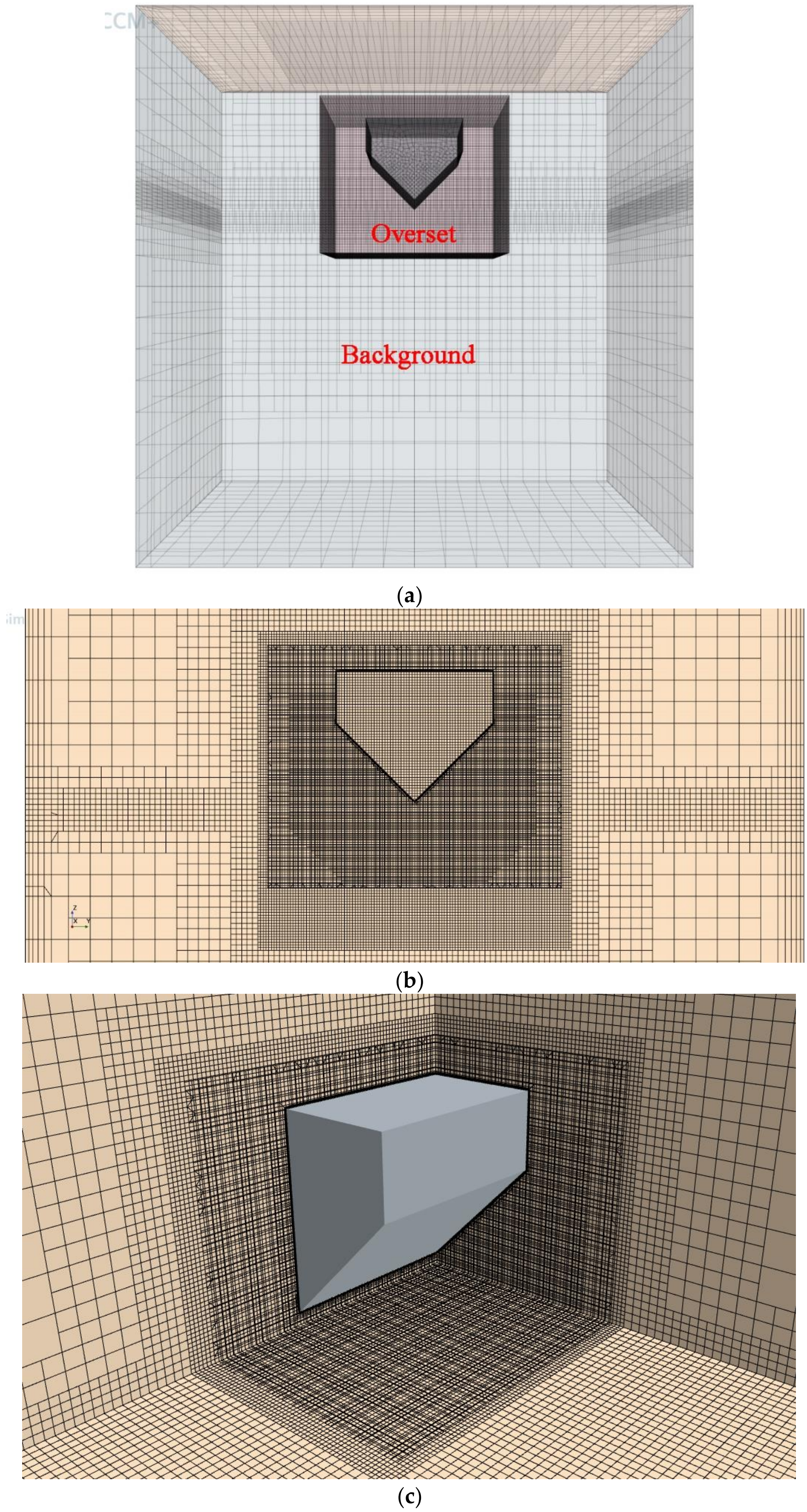

Figure 6. Mesh generation of fluid domain: (**a**) overview of background and overset regions; (**b**) mesh at middle cross-section; (**c**) local mesh refinement around the wedge.

In the numerical simulation, the wedge has the same water entry velocity as the experimental conditions. In order to reduce calculation costs, the wedge is released with an initial speed at a height of H_0 = 50 mm above the calm water surface. This is because the drop process in the air, which is less important, will cost too much time as the calculation frequency is very high. Thus, a corresponding initial speed $V_0 = \sqrt{2g(H - H_0)}$ should be applied on the wedge model. The initial speed for the case of H = 0.1 m, 0.4 m, 0.7 m and 1.0 m height position is V_0 = 0.990 m/s, 2.620 m/s, 3.571 m/s and 4.317 m/s, respectively. In fact, the initial speed is applied in the FEM solver. Only the degree of freedom of vertical displacement of the model is concerned during the numerical simulation.

3.3. The FE Model

The finite element analysis software ABAQUS is used to create an FE model of the wedge structure with stiffeners. The established FE model of the wedge and the mesh generation is shown in Figure 7. In the figure, half a part of the wedge was removed for an improved visualization of the internal local structure. Steel is used to define the material of the FE model, which has the same material properties, such as density, Young's modulus and Poisson ratio, with the experimental model. It is noted that the numerical wedge model was established with certain simplifications compared with the experimental model. The simplified numerical model is closer to a real ship structure. The difference in impact pressure results caused by model simplification is small. To keep the weight of the numerical wedge identical with the experimental one, the thickness of the top plate is set at 25.5 mm, and the side plate is set at 12 mm, which is different from the experimental model.

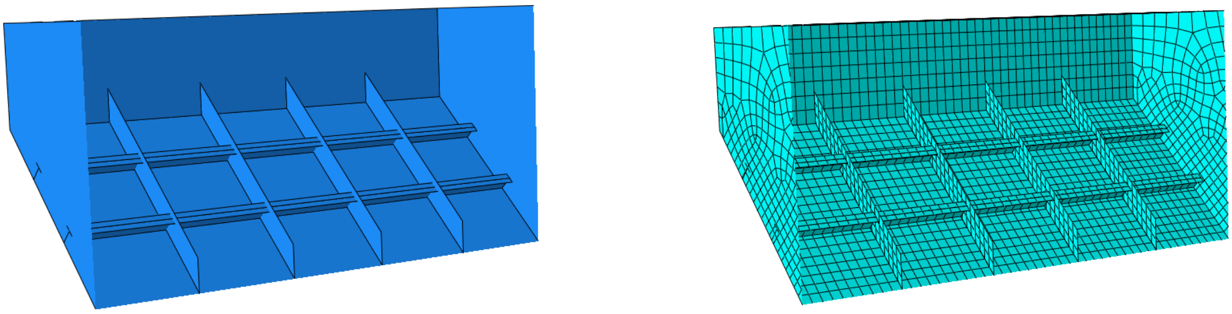

(**a**) (**b**)

Figure 7. FE model of the wedge structure. (**a**) arrangement of local structures. (**b**) mesh generation.

In the FEA, a shell element is applicable when the thickness of plate is much smaller compared with its length and width. Thus, deformable three-dimensional shell elements are used for both the hull plate and stiffened panels of the wedge model. In order to reproduce the welding boundary condition, a constraint of the tie type is used to combine the plate with stiffened panels, including longitudinal and transverse bones, in the interaction module. Loads due to gravity, boundary conditions and predefined velocity fields are all applied to the FE model. The 8-node quadrilateral surface (S8R) is used for modeling the shell elements, while the 4-node quadrilateral surface (S4R) is used for all the stiffeners. The structural surface model was generated by the structured grid, which consists of 5340 elements and 14,424 nodes. The mesh at the bottom of the wedge is locally refined to capture the local stress and improve the accuracy of the numerical results. Only symmetric responses are involved in this study; thus, the wedge model is free to vertically move while constrained in all the other five degrees of freedom by constraining the displacement or rotation of nodes to prevent horizontal interference.

3.4. Two-Way Coupling Configuration

Both STAR-CCM+ and Abaqus have built-in mappers that can be used to transfer pressure loads to the appropriate nodal forces on the structural grid and to project the structural displacements and deformations onto the fluid grid. Although the CFD mesh and the FE mesh represent the same model, their geometry does not match perfectly due to small uncertainties in modeling. This is also because the FE meshes are usually less precise and they are coarser than the CFD meshes.

The external fluid force acting on a FE panel transferred from the CFD solver can be obtained by surface integration. For the case of the structured quadrilateral panel, the area force can be integrated by the isoparametric mapping method with the help of Gauss points. As seen in the example in Figure 8, nine Gauss points are used for each structural panel. A local coordinate system is introduced for Gauss quadrature, and the points are transformed by the Jacobian matrix.

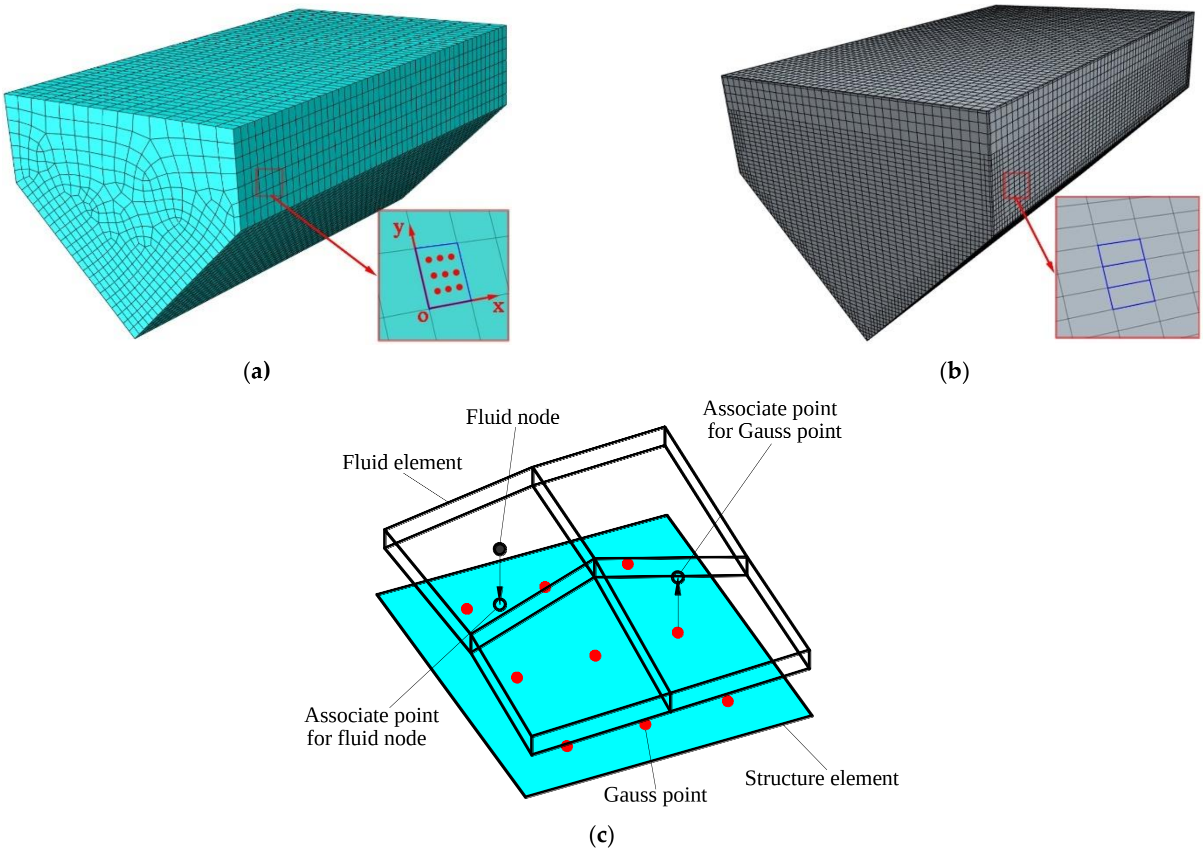

Figure 8. Mesh mapping between CFD and FEM meshes: (**a**) FEM mesh; (**b**) CFD mesh; (**c**) mesh mapping scheme.

Hydrodynamic loads acting on the external surface are converted to nodal forces on the FE model of the wedge structure. Mass inertia forces and moments are also added to nodal forces, allowing computations in a body–fixed coordinate reference frame. The gravity acceleration is applied to the FE model in the whole solution period within the FEA solver, since the hydrodynamic forces from the CFD solver are obtained considering the gravity acceleration.

In this study, the scheme of implicit coupling is adopted to accurately reproduce the hydroelastic responses of slamming and whipping. The number of data exchanges per coupling time step is critical for the stability and accuracy of the partitioned two-way interaction calculations. In this study, the iteration number within each time step is set at four, and three exchanges are performed within each time step. During the numerical simulation, the time step is set at 0.0002 s. The solution time lasts for 0.2 s, which covers the whole water entry process. The CFD–FEM co-simulations are performed by work stations with a single node Intel(R) Core i-9 CPU with 18 cores, a clock speed of 3.0 GHz and 64 GB of physical memory.

To investigate the fluid impact pressure at P1–5 and its distribution, a total of five pressure measurement points are arranged on the CFD model. The structural stress and acceleration at three points S1–3 are measured in the FE model, and the positions of the corresponding node are shown in Figure 9. The vertical speed and displacement of the rigid body movement are also monitored in the FE model.

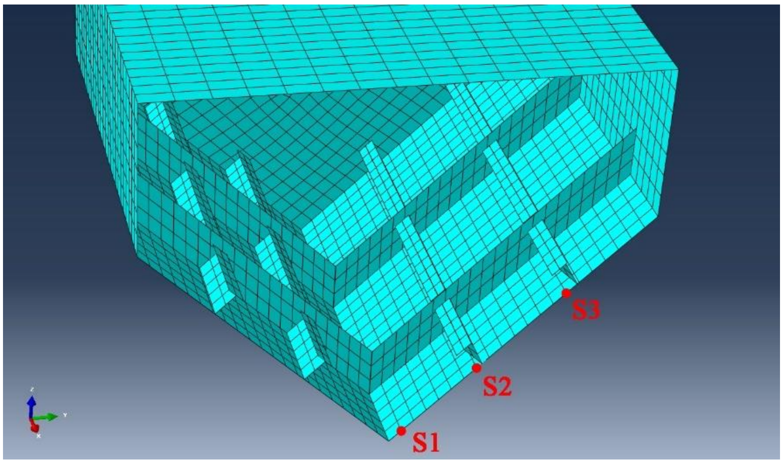

Figure 9. Stress and acceleration monitoring positions on the FE model.

4. Verification of Numerical Results

It is essential to evaluate the precision of the numerical results by performing verification and validation (V&V) analyses. In this section, the numerical uncertainties caused by both CFD and FEM solvers are analyzed. It is known that the uncertainties caused by the modelling and simulation of fluid dynamics by the CFD solver are usually much larger than the uncertainties associated with the structural responses by the FEM solver [34]. Therefore, the influence of the mesh size of the FE model on the results is studied first to confirm this. Then, the uncertainty study is conducted by changing a set of CFD control strategies, such as mesh size and time step, while the FEM scheme is not changed.

4.1. Verification Procedure

The numerical simulation error and uncertainty mainly includes contributions from iteration number, grid size and time step. Previous research has shown that the dependence of the results on inner iteration changes compared to grid and time-step is negligible [35]. Thus, only grid uncertainty (UG) and time step uncertainty (UT) are involved in the present verification study.

The verification procedure proposed in the ITTC [36] is used through convergence studies. The grid and time step convergence studies are performed using three solutions, which are refined systematically with a reasonable refinement ratio $r_i = \sqrt{2}$. $S_{i,1}$, $S_{i,2}$ and $S_{i,3}$ are defined to be the solutions with the fine, medium and coarse input parameters, respectively (for grid uncertainty, analysis *i* is replaced by *G*, and for time step uncertainty analysis, *i* is replaced by *T*). Changes between medium-fine $\varepsilon_{i,21} = S_{i,2} – S_{i,1}$ and coarse-medium $\varepsilon_{i,32} = S_{i,3} – S_{i,2}$ solutions are used to define the convergence ratio:

$$R_i = \varepsilon_{i,21} / \varepsilon_{i,32} \tag{1}$$

Four modes of convergence can occur: (i) when $0 < R_i < 1$, monotonic convergence (MC); (ii) when $-1 < R_i < 0$, oscillatory convergence (OC); (iii) when $R_i > 1$, monotonic divergence (MD) and (iv) when $R_i < -1$, oscillatory divergence (OD). For conditions (iii) and (iv), the numerical uncertainty cannot be estimated. Generally, the preferred state is (i) monotonic convergence, in which case the numerical error $\delta^*{}_{\mathrm{REi},1}$ and order of accuracy p_i can be estimated via the generalized Richardson Extrapolation (RE) approach:

$$\delta^*_{\mathrm{REi},1} = \frac{\varepsilon_{\mathrm{i},21}}{r_\mathrm{i}^{p_\mathrm{i}} - 1} \tag{2}$$

$$p_\mathrm{i} = \frac{\ln(\varepsilon_{\mathrm{i},21}/\varepsilon_{\mathrm{i},32})}{\ln(r_\mathrm{i})} \tag{3}$$

The factor of safety approach is then used to define the uncertainty U_i, where an error estimate from RE is multiplied by a factor of safety F_S = 1.25 to bound simulation error:

$$U_\mathrm{i} = F_S\left|\delta^*_{\mathrm{REi},1}\right| \tag{4}$$

For condition (ii), the numerical uncertainty can be estimated simply by bounding the error within the oscillation of maximum S_U and minimum S_L using the following equation:

$$U_\mathrm{i} = \frac{1}{2}(S_\mathrm{U} - S_\mathrm{L}) \tag{5}$$

4.2. FEM Grid Size Sensitivity

Case 4 (free falling height H = 1.0 m) is used for the uncertainty analyses, as the severest slamming event occurs in this case. To investigate the influence of surface grid size of the FE model on the FSI results, three sets of FEM surface grid are generated for the wedge. A comparative view of the three FEM grid schemes is shown in Figure 10. The mesh density is controlled by mesh seeds assigned along the edge line of the FE model. Table 4 lists the number of mesh seeds on a typical edge, the panel element and the node for each set of grid schemes. In the table, the longitudinal range refers to the longitudinal length of 1500 mm, and the vertical range refers to the broadside height of 300 mm. For the three schemes, the CFD mesh size and time step used is not changed.

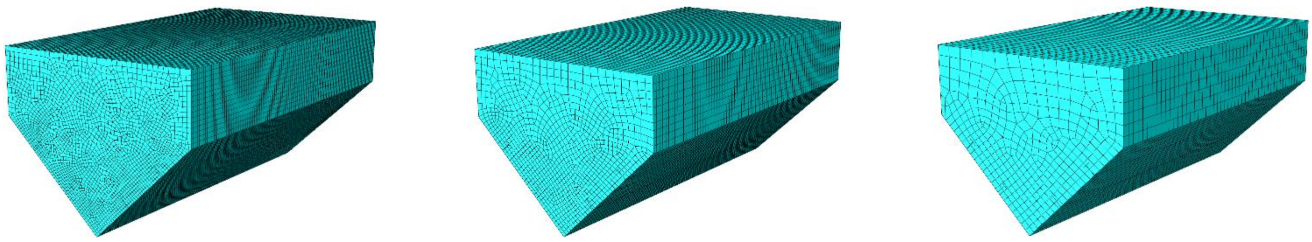

(**a**) (**b**) (**c**)

Figure 10. Comparative view of the three FEM mesh schemes: (**a**) fine mesh; (**b**) medium mesh; (**c**) coarse mesh.

Table 4. Grid parameters of each FEM mesh scheme.

Grid	Mesh Seed Number		Mesh	Nodes
	Longitudinal Range	Vertical Range		
Fine	120	15	31,206	81,528
Medium	80	10	13,386	36,626
Coarse	50	7	5340	14,424

The calculated time series of typical results, including vertical speed, vertical total force, impact pressure at P1 and structural stress at S2, by the three different FEM grid schemes are compared in Figure 11. The results confirm that the structural grid size has very little effect on the simulation results. Thus, the quantitative uncertainty using the ITTC procedure is not conducted. It is noted that there exist slight differences in the structural stress signal, which is mainly caused by the difference in the coordinate position of the target node for different density mesh schemes. It is concluded that the coarse mesh is more efficient compared with the medium and the fine mesh, and it is therefore used for subsequent simulation and calculation.

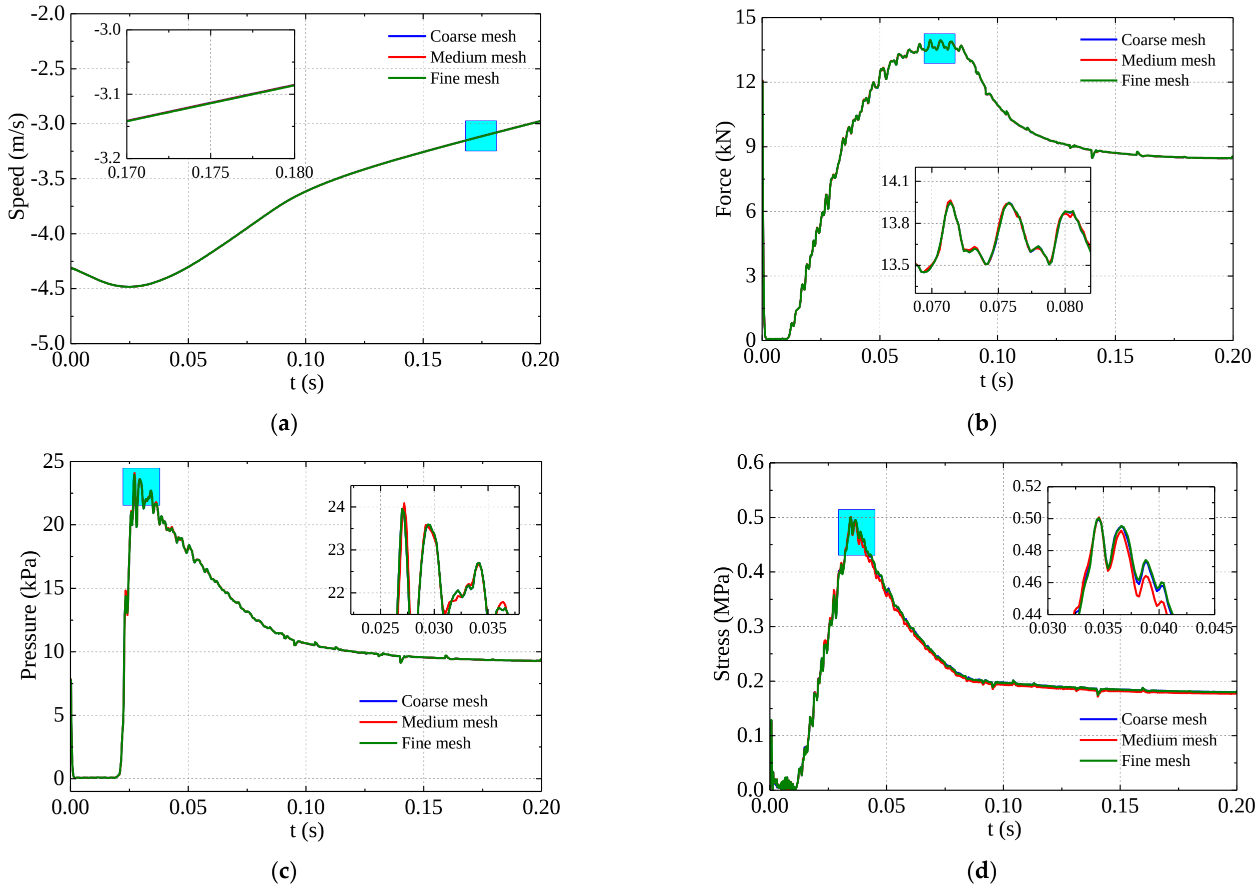

Figure 11. Comparison of time series of slamming results by different FE grid schemes: (**a**) vertical speed; (**b**) vertical total force; (**c**) pressure at P1; (**d**) structural stress at S2.

4.3. CFD Grid Size Sensitivity

To evaluate the grid sensitivity and uncertainty, numerical simulations are carried out with three suites of CFD grids, i.e., fine, medium and coarse. The grid base size of the fine mesh, medium mesh and coarse mesh of the background region are 0.353 m, 0.500 m and 0.707 m, while the minimum size of the fine mesh, medium mesh and coarse mesh are 18 mm, 25 mm and 36 mm, respectively. A comparative view of the three CFD grid schemes is shown in Figure 12. The total number of cells in the fluid domain and the solving time, which corresponds to the time for simulating the ship model response of approximately 0.2 s physically, for each set of the grid scheme are listed in Table 5.

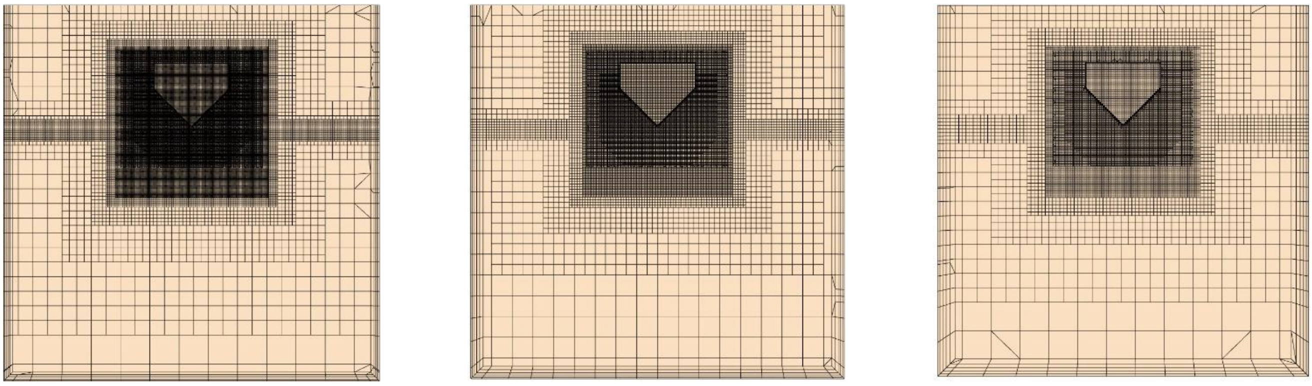

Figure 12. Comparative view of the three CFD mesh schemes: (**a**) fine mesh; (**b**) medium mesh; (**c**) coarse mesh.

Table 5. Grid parameters of each mesh scheme.

Grid	Time Step (s)	Cell Number (Million)			Solving Time (h)
		Background	Overset	Total	
Fine	0.0002	6.93	1.34	8.27	37
Medium	0.0002	2.48	0.53	3.01	21
Coarse	0.0002	0.99	0.21	1.20	14

The time series of vertical total force and impact pressure at P1, P3 and P5 obtained with the three grids are compared in Figure 13. The time-series results indicate that vertical total force and impact pressure at P1, P3 and P5 by the coarse mesh reveals obvious deviation and lower peak value compared with the remaining grids, while the curve representing the fine mesh is the most reasonable one. The verification parameters of load parameters (i.e., vertical total force crest and impact pressure peak) for the grid size convergence study are demonstrated in Table 6. As seen in the table, monotonic convergence (MC) is obtained for impact pressure P1. Oscillatory convergence (OC) is obtained for vertical total force F_z, and impact pressure at P3 and P5. In general, compared with the fine mesh, it is clear that the medium mesh produces similar results and shows higher efficiency.

Table 6. Convergence study for slamming loads by different CFD grid schemes.

Parameter		Force Crest (kN)	Pressure Peak (kPa)		
Description	Symbol	Fz	P1	P3	P5
Fine	S_{G1}	13.92	23.98	20.18	13.61
Medium	S_{G2}	13.96	23.48	19.19	14.36
Coarse	S_{G3}	13.94	23.20	19.53	13.85
Change between Medium-fine	$\varepsilon_{G,21}$	0.04	0.50	0.99	–0.75
Change between Coarse-medium	$\varepsilon_{G,32}$	0.02	0.28	–0.34	0.51
Convergence ratio	R_G	–2.000	1.786	–2.912	–1.471
Convergence type	/	OC	MC	OC	OC
Order of accuracy	p_G	N/A	–1.673	N/A	N/A
Numerical error	$\delta^*_{REG,1}$	N/A	–1.136	N/A	N/A
Uncertainty	U_G	0.02	2.136	0.495	0.375

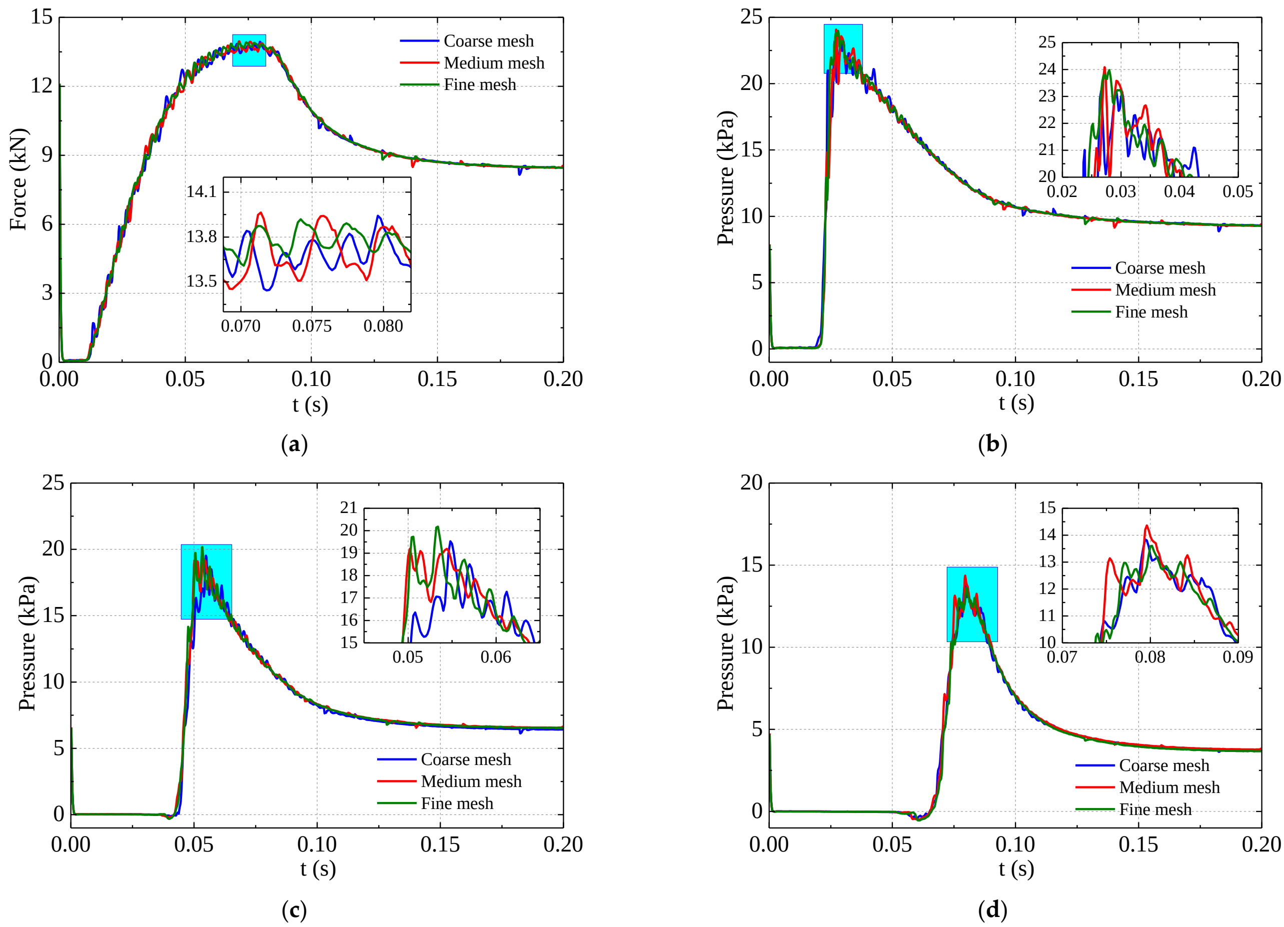

Figure 13. Comparison of time series of slamming results by different CFD grid schemes: (**a**) vertical total force; (**b**) pressure at P1; (**c**) pressure at P3; (**d**) pressure at P5.

4.4. Time Step Sensitivity

The verification analysis for the time step can be conducted similarly. For the simulation of slamming loads, the time step should be small enough so that the high-frequency impact peaks can be exactly captured. The uncertainty analysis of the time step is carried out using three kinds of time step, i.e., small (0.00014 s), medium (0.00020 s) and large (0.00028 s). These three simulations are performed using the medium CFD grid resolution with 3.01 million cells, which is the best choice as a compromise between accuracy and cost in the above analysis.

The time series of the vertical total force F_z and impact pressure at P1, P3 and P5 obtained with the three time steps are compared in Figure 14. The calculation time for the wedge model response to solve approximately 0.2 s of physical time by using the small, medium and large time step schemes is 32 h, 21 h and 15 h, respectively. It can be seen that the influence of the time step on the results, especially the vertical total force, is generally small, and the increase in solving frequency results in a larger impact pressure peak. As shown in the figure, the curve of the medium time step agrees well with that of the small time step. The uncertainty analysis results for the time step convergence study are listed in Table 7. Monotonic convergence (MC) and reasonably small levels of uncertainty are obtained for two of the pressure signals, while the vertical total force is oscillatory convergence (OC).

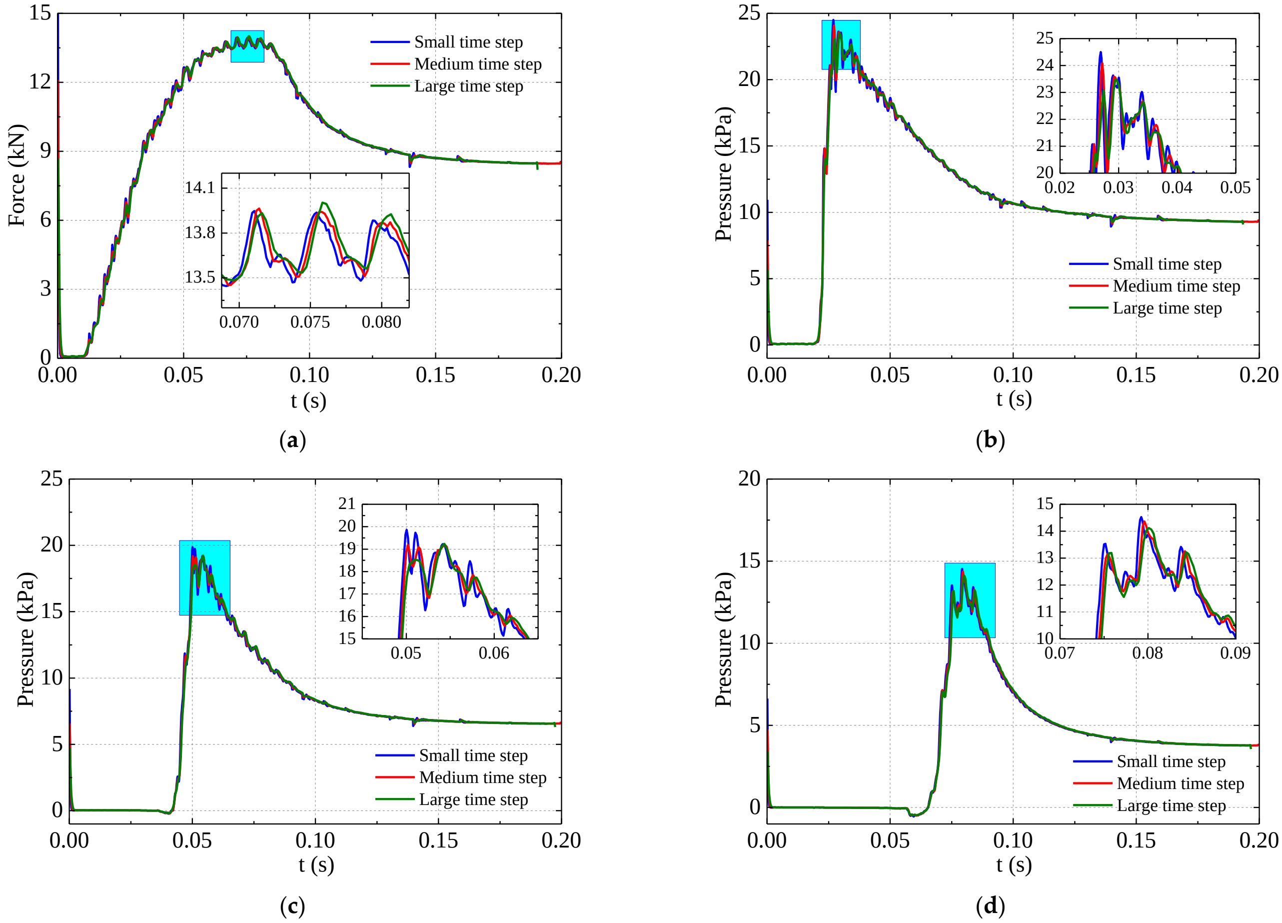

Figure 14. Comparison of time series of slamming results by different time-step schemes: (**a**) vertical total force; (**b**) pressure at P1; (**c**) pressure at P3; (**d**) pressure at P5.

Table 7. Convergence study for slamming results using different time-step schemes.

Parameter		Force Crest (kN)	Pressure Peak (kPa)		
Description	**Symbol**	**Fz**	**P1**	**P3**	**P5**
Small	S_{G1}	16.92	24.50	19.86	14.53
Medium	S_{G2}	13.96	24.09	19.19	14.36
Large	S_{G3}	14.00	23.48	19.24	14.12
Change between Medium-small	$\varepsilon_{G,21}$	2.96	0.41	0.67	0.17
Change between Large-medium	$\varepsilon_{G,32}$	–0.04	0.61	–0.05	0.24
Convergence ratio	R_G	–74.000	0.672	–13.4	0.708
Convergence type	/	OC	MC	OC	MC
Order of accuracy	p_G	N/A	1.146	N/A	0.995
Numerical error	$\delta^*{}_{REG,1}$	N/A	0.8405	N/A	0.4129
Uncertainty	U_G	1.48	0.8405	0.335	0.412857

5. Comparison and Validation of Typical Results

In this section, typical results including displacement, velocity, acceleration, slamming pressure, deformation, structural stresses and total forces on the wedge during the water entry process using the CFD-FEM coupled numerical simulation are presented and analyzed. The numerical results are compared with experimental data for validation purposes. The physical phenomenon and FSI details during the water entry process of the wedge are analyzed.

5.1. Vertical Speed and Displacement

The case of No. 4 (free falling height H = 1.0 m) is used for illustrative analysis, as the severest slamming occurred in this case due to relative high impact speed. Figure 15 shows the vertical speed and displacement of the wedge during the water entry process in the comparison between numerical and experimental results. It can be seen that the vertical speed increases initially, as the gravity is greater than the fluid resistance. In the numerical results, the largest speed of 4.482 m/s occurs at 24.2 ms; then, the speed decreases gradually due to large impact force. The slamming event occurs during the period from approximately 0.012 s to 0.095 s, which is identified from the curves of vertical force and pressures at different points. After 0.095 s, the reduction rate of speed decreases as the speed trend is small and steady.

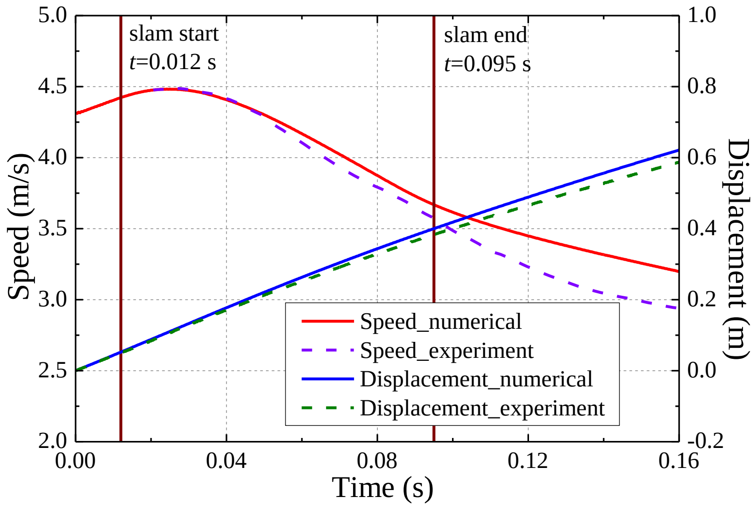

Figure 15. Comparison of vertical speed and displacement by simulation and experiment (Case 4).

In the figure, the numerical results are compared with the experimental data. The difference between numerical and experimental data in vertical displacement is initially small but increases gradually. The slamming process takes place in the period from 0 to approximately 0.1 s, during which the difference in vertical displacement is small and acceptable. Although the difference in vertical displacement is pronounced after 0.1 s, this is not problematic, as this period is less concerning, the speed is small and the slamming event has already taken place. Generally, the vertical speed by experiment is slightly smaller than the numerical value, but the difference is less than 3.5% in the period from 0 to 0.1 s.

Figure 16 shows the simulated fluid flow and structural stress distribution on the wedge at six typical time instants during water entry process. The figure shows that when the wedge enters the water, the static flow field is severely disturbed, resulting in a large slamming pressure as long as the structural stress acting on the surface of the wedge. Specifically, the stress caused by slamming propagates from the bottom of wedge to the bilge region. However, large stress occurs at the bottom of the wedge, especially on the transverse frames during the whole process. From the volume fraction of water distribution at the middle plane of the wedge, as shown in Figure 16a, water pile-up of the free surface can be seen. Prior to contact water, the instantaneous peak stress on the wedge is around 10 MPa, which occurs on the bottom of the wedge, while the stress on the transverse frames is nearly 5 MPa, which is half of the maximum stress. With the increase of water entry depth, the stress on the plate increases gradually, while the stress at the bottom plate increases sharply and reaches the largest value of 41 MPa. The maximum stress is stable around 23 MPa after 0.12 s. When the wedge impacts with the water surface, the surrounding water spreads away rapidly, forming a jet flow and water pile-up phenomenon.

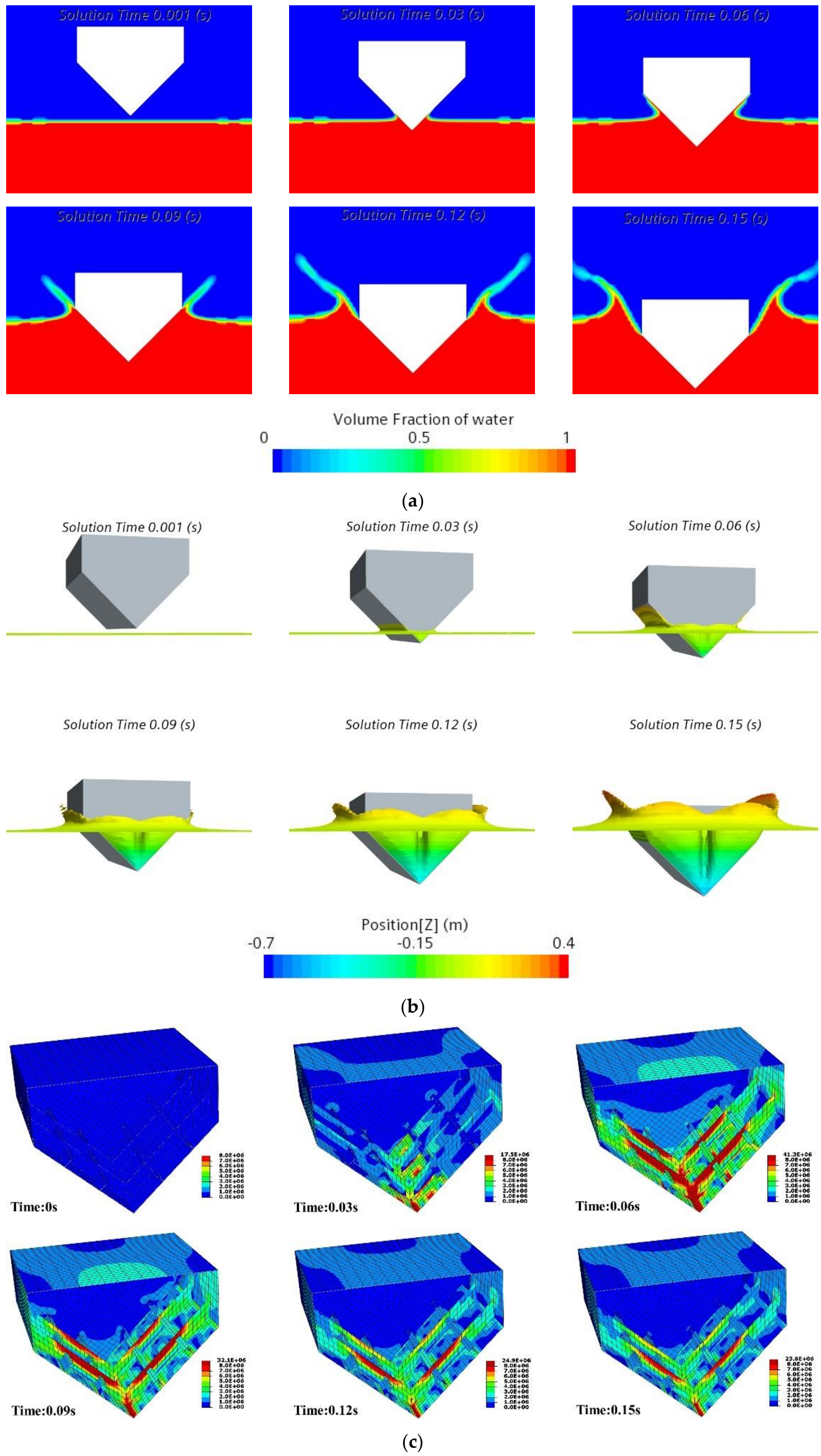

Figure 16. Visualization of FSI results during water entry procedure (Case 4): (**a**) volume fraction of fluid domain; (**b**) free surface around the wedge; (**c**) structural stress distribution on the wedge.

A comparison of the free surface flow around the wedge during the water entry process between the numerical simulation and experiment is shown in Figure 17. It confirms that the CFD solver is able to simulate and capture flow details such as the fluid separation and jet phenomena caused by slamming of the wedge. In the experiment, very obvious breaking and splashing of water pile-up and jet flow took place. This was, however, not well captured by the CFD solver due to the inherent limitation of the mesh-based tool. In future work, a meshless or particle method such as SPH and MPS can be used to reproduce the splashing of water for better flow details.

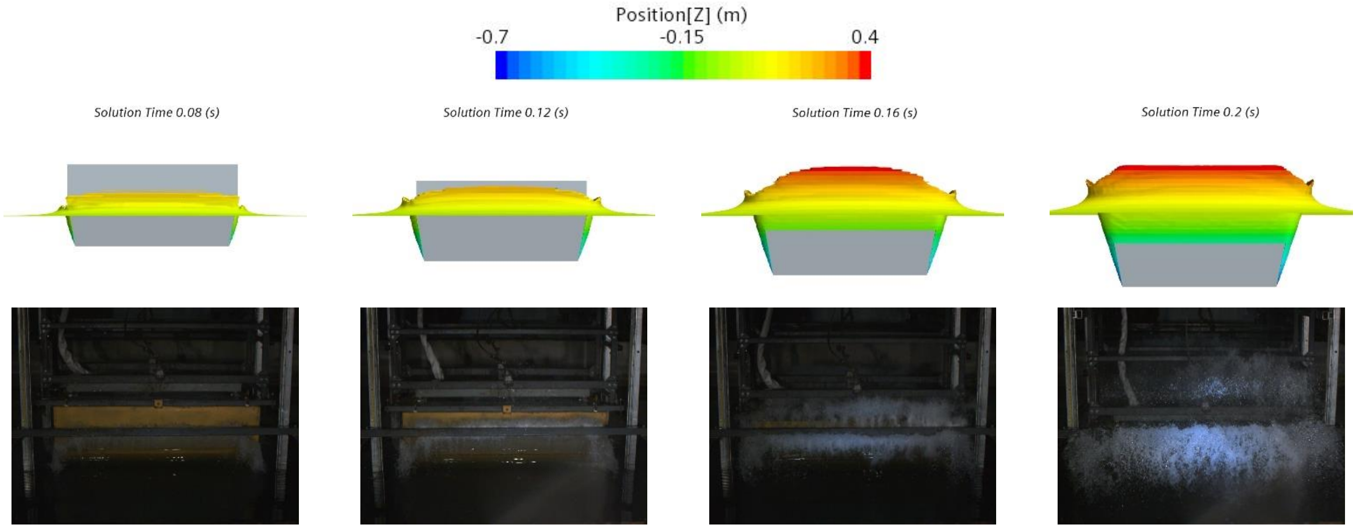

Figure 17. Comparison of experimental and numerical flow phenomena at different times (Case 4).

5.2. Impact Pressure

Figure 18 shows the impact pressure at P1–5 by both numerical and experimental methods. To remove high-frequency noise from the original data, the impact pressure data were low-pass filtered with a cut-off frequency of 200 Hz. Note that the sampling frequency is 5000 Hz and 10,000 Hz for the numerical simulation and experiment, respectively. It can be seen that the numerical simulation and experiment results show a similar tendency, and the largest peak occurs at P1 due to the largest vertical speed. The impact pressure peak decreases from P1 to P5 for both the numerical and experimental results. There are some fluctuations in the pressure curve due to the fluid disturbance. It can be seen that negative pressure occurred prior to the slamming event. This is caused by the rapid flow of air due to movement of the wedge, which resulted in a low pressure area.

Table 8 lists the duration of the slamming event at different points P1–5 of the numerical simulation and experiment, denoting the time duration from the start of the impact slam to the peak time. It is seen that the slamming duration increases from P1 to P5 due to the decrease of impact speed. The difference between numerical and experimental slamming duration at P1 is large (47.4%) due to the strong nonlinearity and randomness at the high slamming speed, while for P2–5, the difference is below 20%.

Table 8. Comparison of slamming duration (ms).

Point	P1	P2	P3	P4	P5
Numerical	11.2	12.4	16.4	18.2	23.8
Experiment	7.6	14.2	17.3	22.1	29.7
Difference	47.4%	–12.7%	–5.2%	–17.6%	–19.9%

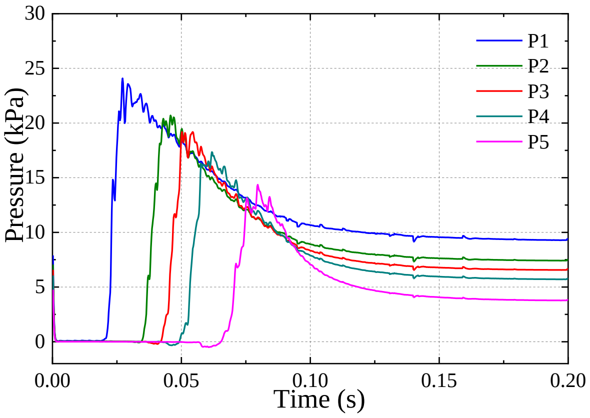

(**a**)

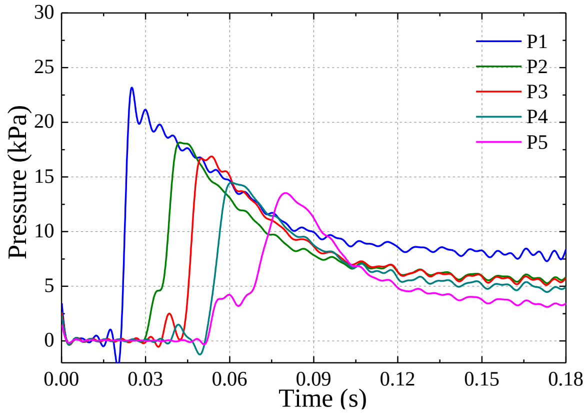

(**b**)

Figure 18. Impact pressure at P1–5 by different methods (Case 4): (**a**) numerical results; (**b**) experimental results.

Furthermore, the comparison of impact pressure between numerical simulation and the experiment at three typical positions, P1, P3 and P5, is shown in Figure 19. It can be seen that the numerical results of impact pressure show a similar trend to the experimental results. However, there are more fluctuations around the peak of the slamming pressure obtained by numerical simulation. The slamming pressure peak obtained by numerical simulation is generally a little larger than the experimental data for all the points.

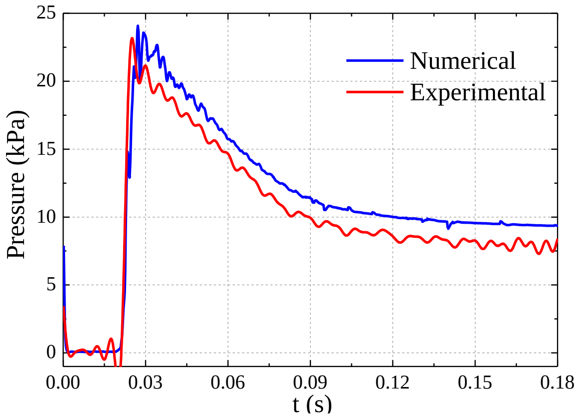

(**a**)

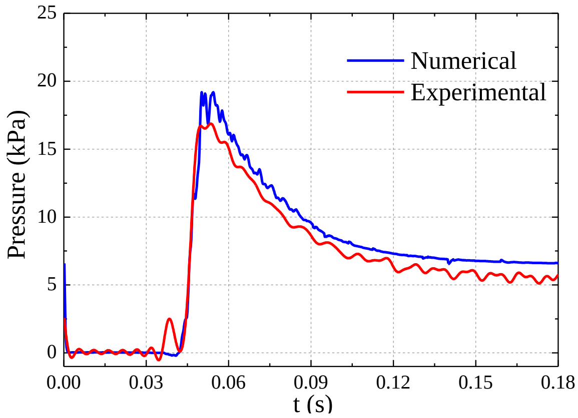

(**b**)

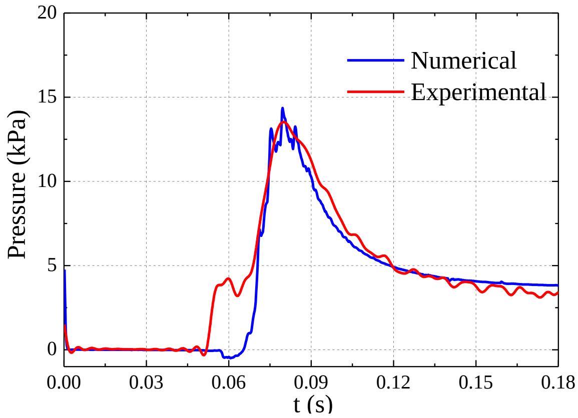

(**c**)

Figure 19. Comparison of impact pressure by simulation and experiment (Case 4): (**a**) impact pressure at P1; (**b**) impact pressure at P3; (**c**) impact pressure at P5.

Table 9 summarizes the comparative pressure peak data at different points by different methods. It is found that the peak values in the experiment are generally smaller than the numerical values, with a difference in the range of 3.97–19.74%. The experimental peak occurs slightly prior to the numerical peak. The difference between the experiment and numerical simulation could be caused by the difference in the mass distribution and local structural stiffness due to the simplification of the numerical model.

Table 9. Comparison of slamming peak value by different methods (Case 4).

Point		P1	P2	P3	P4	P5
Time (s)	Numerical	0.0272	0.0458	0.0544	0.0618	0.0796
	Experiment	0.0251	0.0422	0.0535	0.0607	0.0799
Pressure (kPa)	Numerical	24.09	20.70	19.19	17.35	14.36
	Experiment	23.17	18.15	16.88	14.49	13.53
	Error	3.97%	14.05%	13.68%	19.74%	6.13%

Figure 20 shows the variation of pressure distribution around the wedge and in the fluid domain during the water entry process. The largest impact pressure appears at the bottom of the wedge near the time instant 0.04 s, where the largest vertical speed occurs. In the following time instants, the pressure distribution on the wetted surface of the wedge trends small due to the decrease of speed. According to the empirical formula proposed by von Karman [4] and Wagner [5], the impact pressure at any position is determined by the relative speed and deadrise angle. So, the pressure distribution on the wetted surface of the wedge is theoretically identical at a same time instant. However, there is an increasing trend in pressure distribution from the top to bottom of the wetted surface of the wedge's bottom, mainly due to the hydrostatic pressure component.

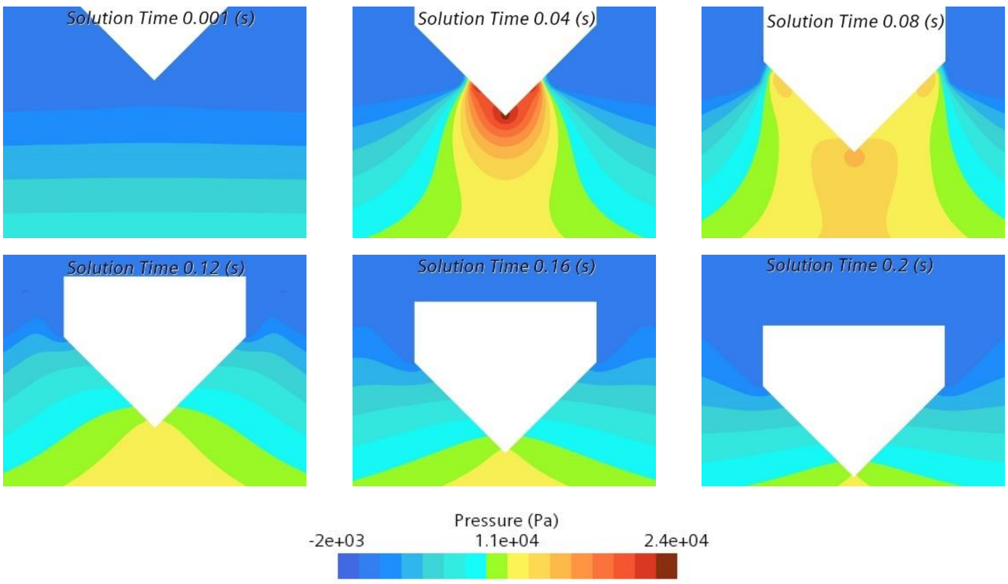

Figure 20. Pressure distribution of fluid domain at different time (Case 4).

5.3. Structural Stress and Acceleration

Figure 21 shows the structural stress at bottom points S1–3 during the water entry process. Both the time series and spectra obtained by fast Fourier Transform (FFT) are presented. The largest structural stress occurs at position S2, while the lowest stress occurs at S3. The stress magnitude is determined by not only external fluid loads but also local structural details, such as plate thickness and arrangement of stiffeners. The ordinate of the stress spectra is given in LOG scale to show the high-frequency components. It is clear that there are obvious high-frequency whipping loads that superposed on the low-frequency stress loads due to structural elasticity effects.

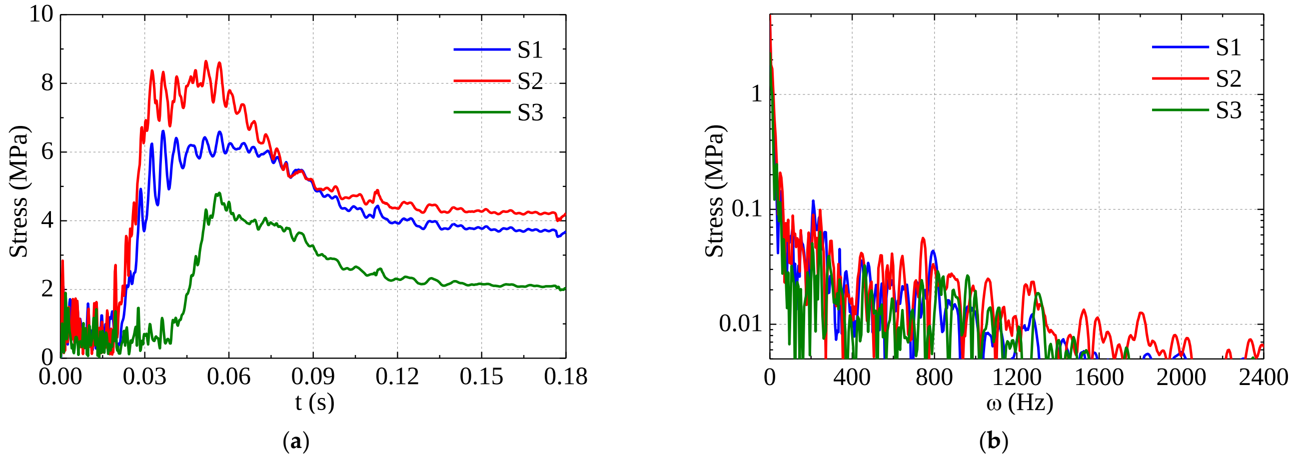

Figure 21. Structural stress at points S1–3 (Case 4): (**a**) time series; (**b**) frequency spectra.

Moreover, the vertical acceleration at bottom points S1–3 during the water entry process is shown in Figure 22a,b. It is seen that in the time series, the high-frequency vibrations are very pronounced initially, which is probably caused by numerical dispersion. Then, the acceleration tends to be steady, and small amplitude whipping loads are superposed on the low-frequency signal. As seen from the spectra, there exist several peaks, which represent different natural frequencies of various types of vibration modes. In order to understand the vertical vibration modal behavior, the numerical simulation is further conducted by releasing only one degree of freedom (i.e., vertical displacement) of all the FE nodes. The corresponding acceleration results of both time series and frequency spectra are shown in Figure 22c,d. It is seen that the first three orders of natural frequency of vertical vibration, 1202 Hz, 1334 Hz and 1670 Hz, can be clearly identified from the frequency spectra curves.

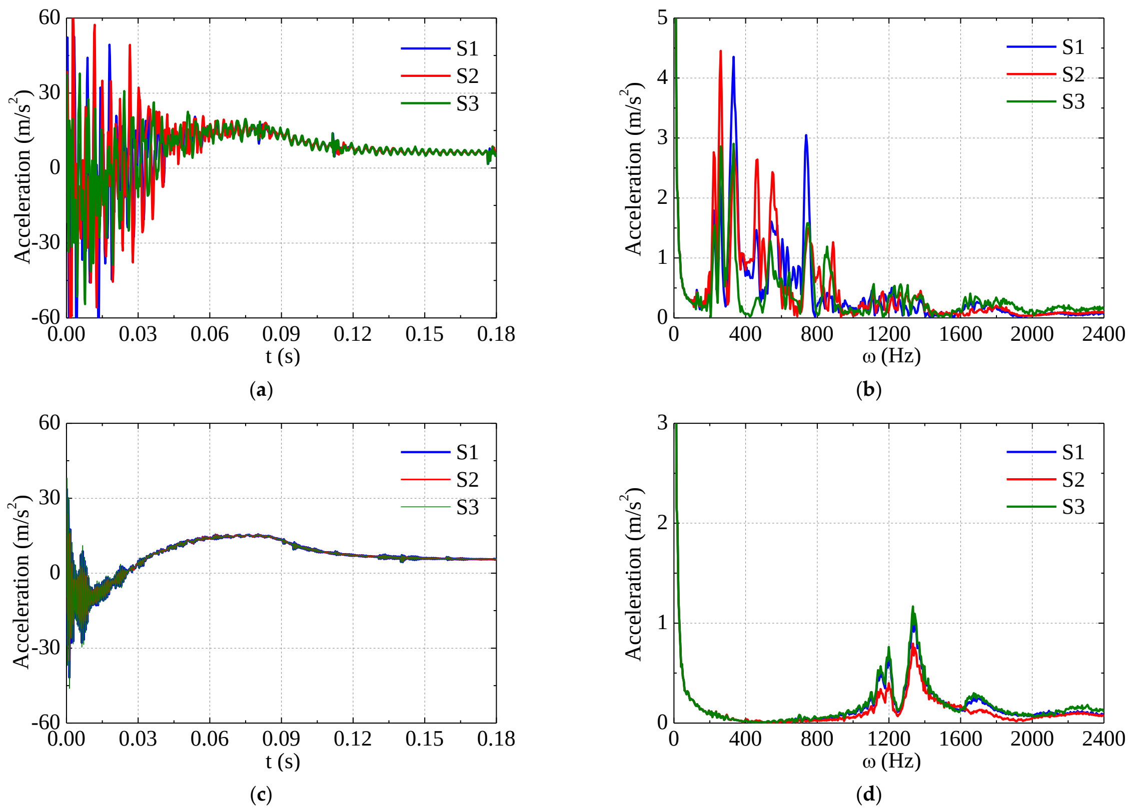

Figure 22. Vertical acceleration at points S1–3 (Case 4): (**a**) time series for 6-DOF released; (**b**) spectra for 6-DOF released; (**c**) time series for 1-DOF released; (**d**) spectra for 1-DOF released.

Figure 23 shows the structural stress distribution on the wedge surface during the water entry process as simulated by the FEM solver. The high stress area occurs at the bottom of the wedge and on the transverse frame, and the high stress area spreads upwards with the increase of the water entry depth. The structural stress tends to be small after 0.12 s because the slamming effect is not pronounced. The stiffeners largely contribute to the structural strength of the plate on the grillage structure. The stress on the transverse frame is larger compared with that on the T-profile, likely due to the smaller section modulus. Since the wedge structure has relatively large stiffness, and the impact is not very severe, the largest stress on the structure is at an appropriate level of about 41 MPa, which is much smaller than the yield strength level. Figure 24 shows the structural deformation of the grillage structure (enlarged 1200 times for an obvious visualization). The deformation of the T-profile is more pronounced than the transverse frame.

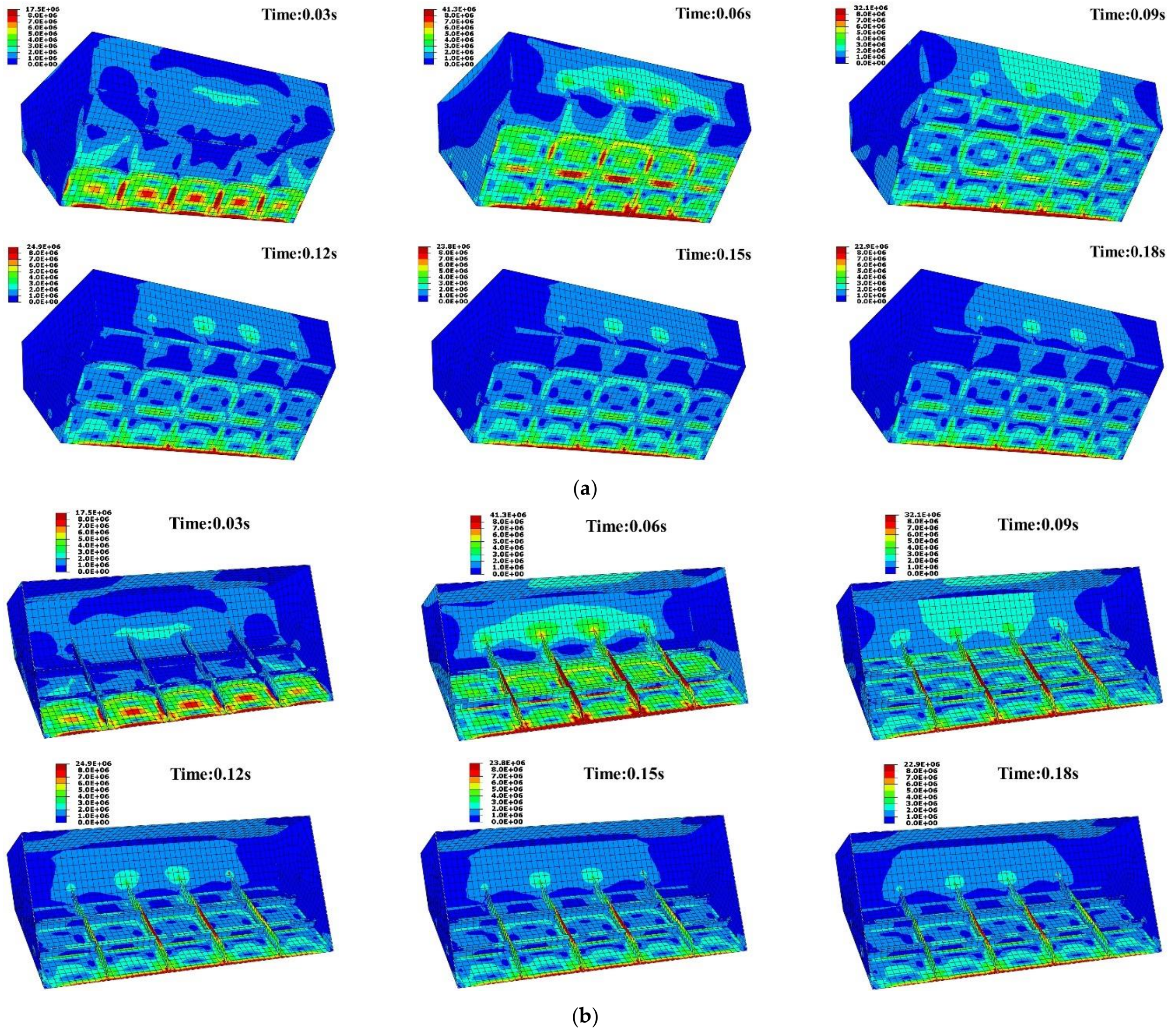

Figure 23. Structural stress distribution on the wedge structure (in MPa): (**a**) overview of the external surface; (**b**) overview of the internal grillage structure.

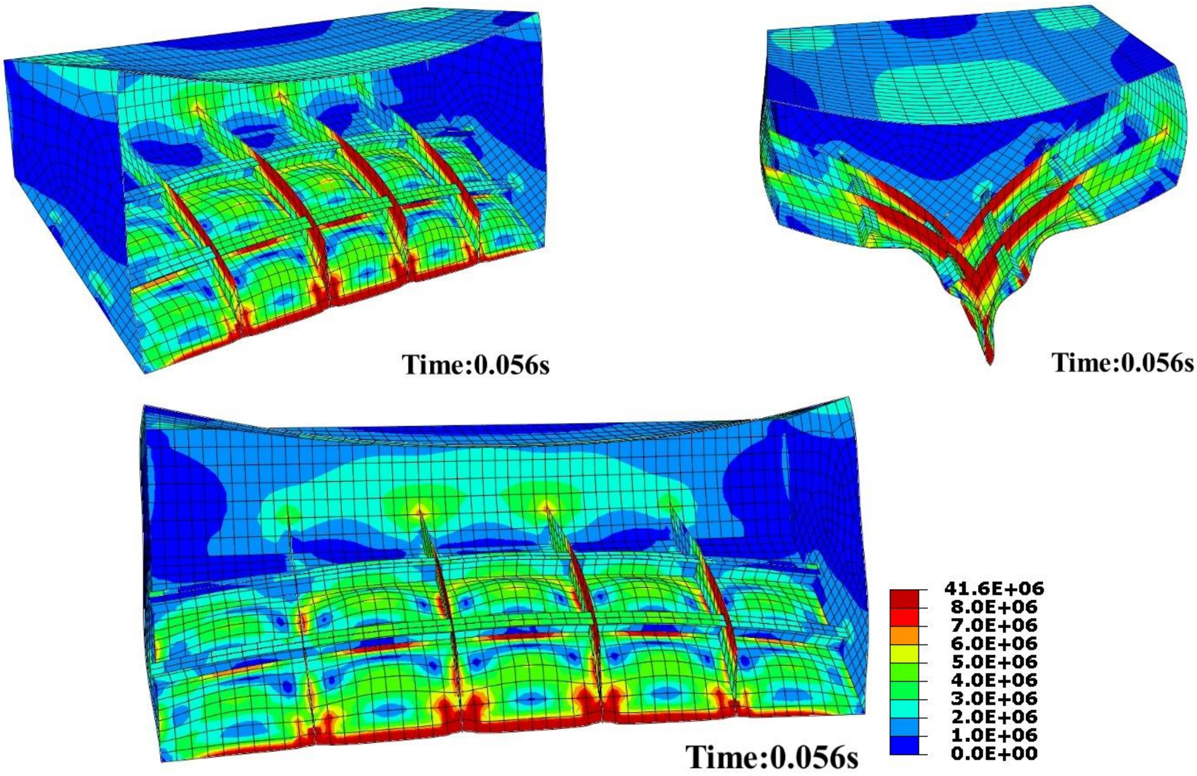

Figure 24. Structural deformation of grillage structure (in MPa; deformation enlarged 1200 times).

6. Slamming Results of Different Water Entry Velocities

In this section, the numerical simulation results of the wedge under different conditions are presented. The influence of impact speed on the results of FSI behavior is analyzed and discussed.

6.1. Vertical Speed and Displacement

Figure 25 compares the time series of vertical displacement and speed at different free falling heights of H = 0.1 m, 0.4 m, 0.7 m and 1.0 m by numerical simulation. The four displacement curves show different tendencies. The curve becomes steeper with the increase of free falling height. The vertical displacement at the time instant 0.2 s is 0.354 m, 0.562 m, 0.668 m and 0.745 m for Case 1 to 4, respectively. The vertical speed increases initially and then decreases due to fluid impact force. The maximum speed occurs earlier with increasing free falling height from Case 1 to 4. Table 10 lists the comparison of speed information between numerical simulation and experiment for different free falling heights. For the majority of the cases, the initial vertical speed when contacting water and the maximum speed during the water entry process by numerical simulation are slightly larger compared with the experimental data.

Table 10. Comparison of speed information at different free falling heights.

Case		1	2	3	4
Free falling height (m)		0.1	0.4	0.7	1.0
Time of contacting water (ms)		41.8	18.4	13.6	11.4
Initial speed when contacting water (m/s)	Numerical	1.396	2.793	3.695	4.417
	Experiment	1.339	2.684	3.773	4.274
	Error	4.26%	4.06%	–2.07%	3.35%
Maximum speed during water entry (m/s)	Numerical	2.143	3.014	3.803	4.482
	Experiment	2.013	2.696	3.797	4.322
	Error	6.46%	11.79%	0.16%	3.70%

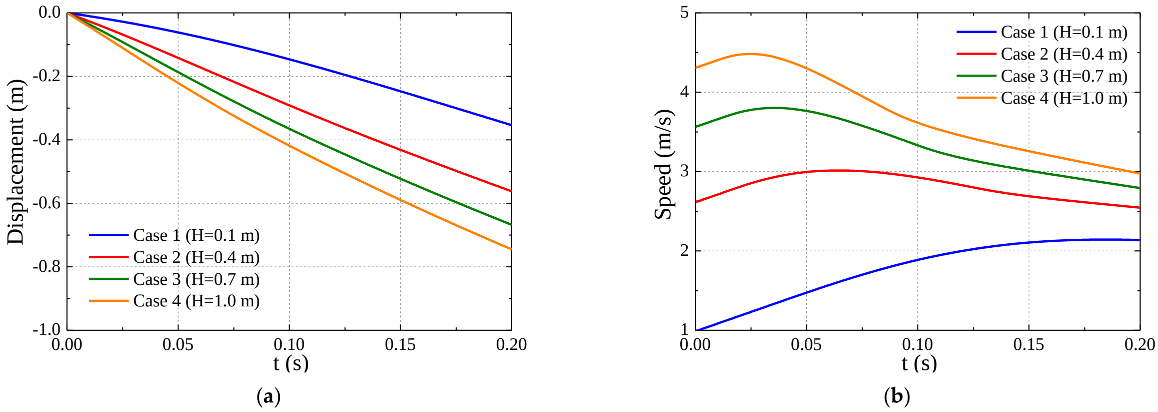

Figure 25. Vertical displacement and speed at different free falling heights: (**a**) displacement; (**b**) speed.

6.2. Impact Pressure and Total Force

Figure 26 shows the vertical total force and impact pressure at typical points of P1, P3 and P5 for different free falling height cases. It is seen that the vertical total force appears after the wedge's bottom contacts the water. Then, the vertical total force increases rapidly with the increase of water entry depth. The climbing range of vertical total force curve lasts for a relatively long period, and its crest is gentle and smooth, which is different from the impact pressure curves. The slope of the vertical total force curve in the declining range tends to be steeper from Case 1 to 4. Note that the vertical total force of Case 1 increases throughout the duration, as the speed increases during this period. The slope of the impact pressure curve in the climbing range is steeper for higher free falling heights due to larger peak value and shorter slamming duration. For Case 1, the slamming peak does not appear due to the low impact speed, which indicates that the slamming only occurs when the relative speed exceeds a critical value.

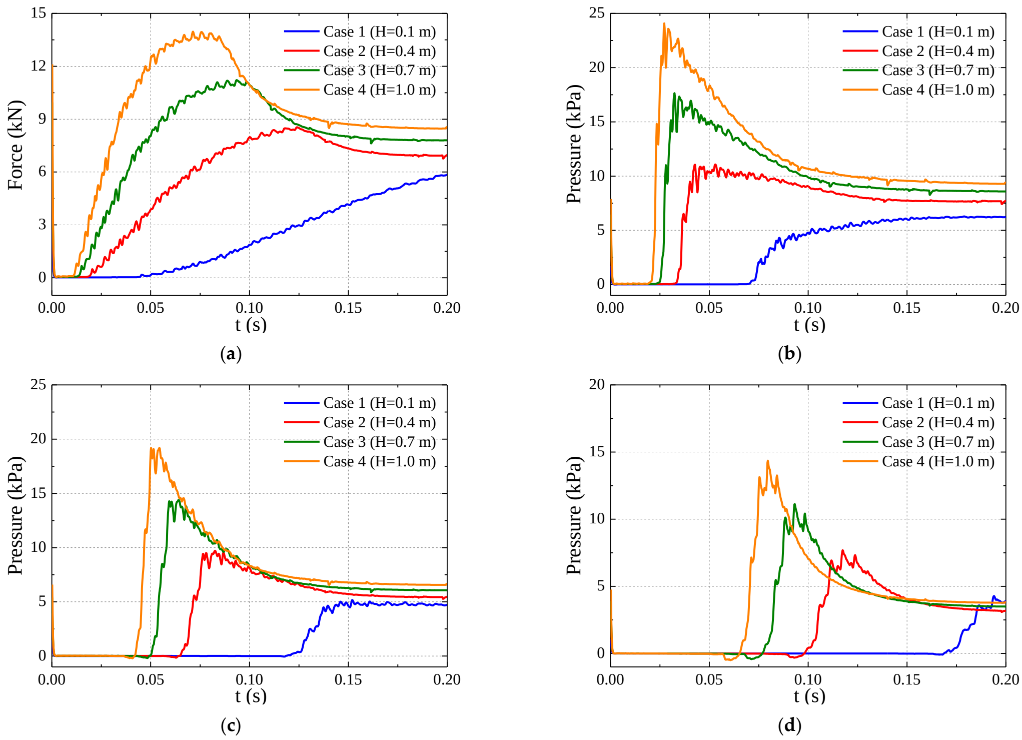

Figure 26. Impact force and pressure at different free falling heights: (**a**) vertical total force; (**b**) impact pressure at P1; (**c**) impact pressure at P3; (**d**) impact pressure at P5.

Table 11 summarizes the impact pressure results under different conditions. The results include the peak pressure P, the instantaneous vertical speed V, and the resulting dimensionless impact factor represented by the formula $k = 2P/\rho V^2$, where ρ denotes water density. The dimensionless impact factor k, varying with different cases, is shown in Figure 27. According to the empirical formula, the dimensionless impact factor k at a specific point mainly depends on the sectional shape, especially the local dead-rise angle, though it is independent of speed. The results are generally in agreement with this rule, but the dimensionless impact factor shows a slightly decreasing tendency with the increase of impact speed, especially for P1, which is located near the bottom of the wedge. Moreover, the dimensionless impact factor increases for points from the top to the bottom. This is likely caused by the coupled effects of strongly nonlinear hydrodynamics and aerodynamics at the initial water entry stage.

Table 11. Summary of impact pressure results.

Case		1	2	3	4
P1	Pressure (kPa)	6.275	11.077	17.651	24.089
	Speed (m/s)	2.142	3.003	3.800	4.480
	k	2.735	2.457	2.445	2.400
P2	Pressure (kPa)	5.308	10.612	15.744	20.697
	Speed (m/s)	2.111	3.012	3.742	4.351
	k	2.382	2.339	2.249	2.187
P3	Pressure (kPa)	5.166	9.715	14.395	19.190
	Speed (m/s)	2.110	2.989	3.672	4.300
	k	2.321	2.175	2.135	2.076
P4	Pressure (kPa)	4.862	9.206	13.314	17.347
	Speed (m/s)	2.137	2.955	3.598	4.143
	k	2.129	2.109	2.057	2.021
P5	Pressure (kPa)	4.276	7.692	11.128	14.364
	Speed (m/s)	2.141	2.842	3.400	3.880
	k	1.866	1.905	1.925	1.908

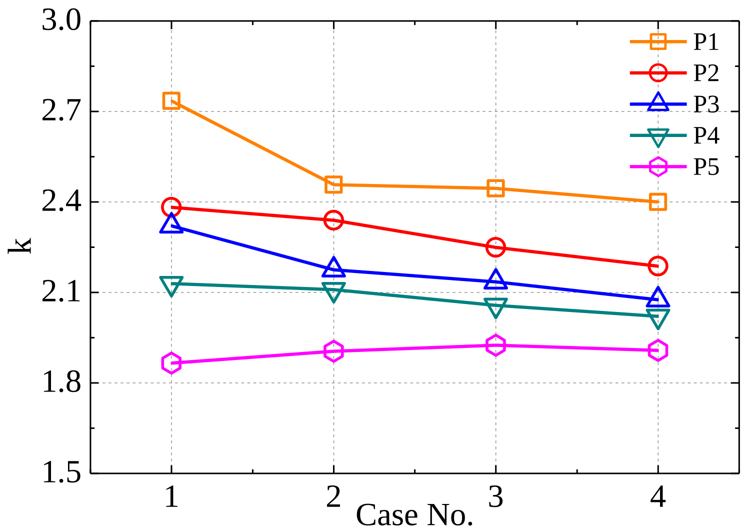

Figure 27. Distribution of dimensionless impact factor k.

6.3. Structural Stress and Acceleration

Figure 28 shows the structural stress at bottom point S2 during the water entry process for different free falling height cases. Point S2 is used for illustration, as the largest stress occurs on it among points S1–3. It is seen that the stress crest increases, and the high-frequency whipping load is more pronounced with higher falling height cases. The high-frequency whipping concentrates around the crest of the stress curve. The high-frequency whipping is weak for Case 1 due to weak slamming effects. The ordinate of stress spectra is given in LOG scale to show the high-frequency components. The high-frequency loads are distributed over a wide frequency range.

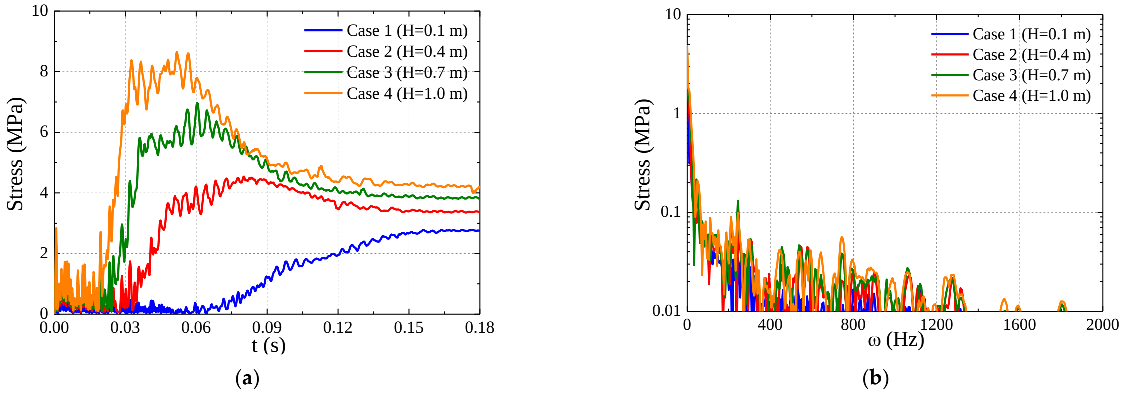

Figure 28. Structural stress at different cases (at Point S2): (**a**) time series; (**b**) frequency spectra.

Figure 29 shows the vertical acceleration at bottom point S2 during the water entry process for different free falling height cases. Figure 29a,b shows the time series and frequency spectra for the case of 6-DOF released of all the FE nodes. The high-frequency components distribute at the same frequency bands for different falling height cases. The high-frequency whipping response is more obvious for the case of higher falling height. To identify the vertical vibration mode, Figure 29c,d shows the time series and frequency spectra obtained by simulation of only 1-DOF of vertical displacement released. The first three orders of natural frequency of vertical vibration can be clearly identified from the frequency spectra curves.

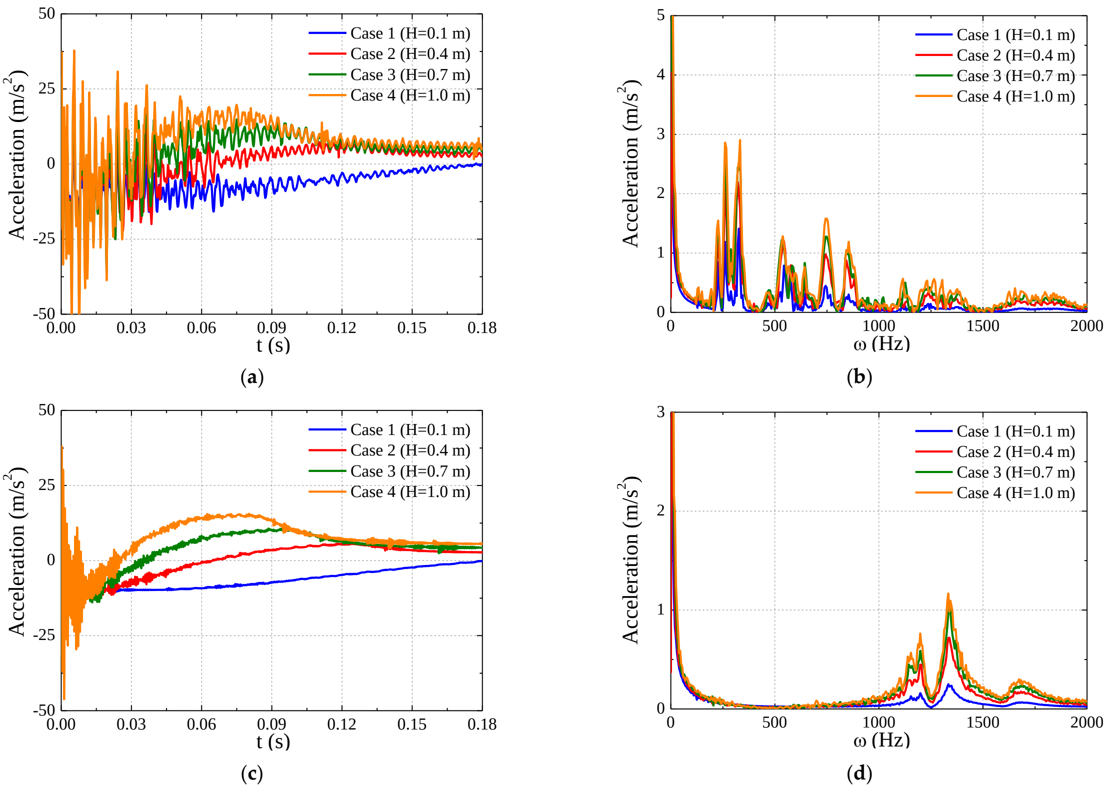

Figure 29. Vertical acceleration at different cases (at Point S2): (**a**) time series for 6-DOF released; (**b**) spectra for 6-DOF released; (**c**) time series for 1-DOF released; (**d**) spectra for 1-DOF released.

7. Conclusions

In this paper, a CFD–FEM two-way coupled method was used to simulate the water entry process of the wedge structure in a numerical tank. Verification and validation of the numerical results were conducted. Almost all the physical characteristics of interest within the scope of water impact and structural response could be satisfactorily reproduced by the presented CFD-FEA co-simulation approach. Therefore, it is believed that this method has wide application value in slamming simulations. The following conclusions can be drawn.

(1) The verification analyses indicated that the uncertainties caused by the modelling and simulation of fluid dynamics by the CFD solver were usually much larger than the uncertainties associated with the structural responses by the FEM solver. The structural grid size of the FE model had very little effect on the simulation results, even though the FE grid is much coarser than the CFD grid.

(2) The vertical speed from the experiment was slightly smaller than the numerical value, with a difference of less than 3.5% in the period when slamming occurs. The slamming pressure peak obtained by numerical simulation was generally a little larger than the experimental data. The dimensionless impact factor depended on the sectional shape, especially the empirical local dead-rise angle. However, in the experimental results, it increased for points from top to bottom. This was likely caused by the coupled effects of strongly nonlinear hydrodynamics and aerodynamics at the initial water entry stage.

(3) The high-frequency whipping responses in the stress and acceleration were well reproduced by the CFD-FEM coupled method, indicating that the structural elasticity and related responses could be fully considered. The high-frequency components at different positions of the wedge structure and for different falling height cases were distributed at the same frequency bands.

Author Contributions: Conceptualization, Z.C. and J.J.; methodology, Z.C. and J.J.; software, Z.C.; validation, Q.W.; formal analysis, Z.C. and J.J.; investigation, Z.C. and J.J.; writing—original draft preparation, J.J.; writing—review and editing, Z.C. and S.W.; visualization, Z.C. All authors have read and agreed to the published version of the manuscript.

Funding: This research is supported by the National Natural Science Foundation of China (Nos. 52271316 and 51909096), the State Key Laboratory of Coastal and Offshore Engineering at Dalian University of Technology (No. LP2102), the Guangdong Basic and Applied Basic Research Foundation (No. 2022A1515010453) and the Science and Technology Project in Guangzhou, China (No. 202102020899).

Institutional Review Board Statement: Not applicable.

Informed Consent Statement: Not applicable.

Data Availability Statement: All data, models, or code generated or used during the study are available from the corresponding author by request.

Acknowledgments: The authors would like to thank the members of Huilong Ren's research team at Harbin Engineering University who participated in the wedge slamming experiment for making the experimental data available for use and for numerical validation.

Conflicts of Interest: The authors declare no conflict of interest.

References

1. Kapsenberg, G.K. Slamming of ships: Where are we now? *Phil. Trans. R. Soc. A* **2011**, *369*, 2892–2919. [CrossRef] [PubMed]
2. Wang, S.; Guedes Soares, C. Experimental and numerical study of the slamming load on the bow of a chemical tanker in irregular waves. *Ocean Eng.* **2016**, *111*, 369–383. [CrossRef]
3. Jiao, J.L.; Ren, H.L. Characteristics of bow-flare slamming and hydroelastic vibrations of a vessel in severe irregular waves investigated by segmented model experiments. *J. Vibroengineering* **2016**, *18*, 2475–2494. [CrossRef]
4. Von Karman, T. The Impact on Seaplane Floats During Landing. NASA TN-321, 1 October 1929. Available online: https://ntrs.nasa.gov/api/citations/19930081174/downloads/19930081174.pdf (accessed on 20 August 2022).
5. Wagner, V.H. Phenomena associated with landing and sliding on liquid surfaces. *Natl. Advis. Comm. Aeronaut.* **1932**, *321*, 145–162.
6. Xu, G.; Duan, W. Review of prediction techniques on hydrodynamic impact of ships. *J. Mar. Sci. Appl.* **2009**, *8*, 204–210. [CrossRef]

7. Cumberbatch, E. The impact of a water wedge on a wall. *J. Fluid Mech.* **1960**, *7*, 353–374. [CrossRef]
8. Zhao, R.; Faltinsen, O.M. Water entry of two-dimensional bodies. *J. Fluid Mech.* **1993**, *246*, 593–612. [CrossRef]
9. Faltinsen, O.M. Water entry of a wedge by hydro-elastic orthotropic plate theory. *J. Ship Res.* **1999**, *43*, 180–193. [CrossRef]
10. Watanabe, I. Theoretical investigation on the wave impact loads on ships. In Proceedings of the 16th Symposium on Naval Hydrodynamics, Bekeley, CA, USA, 13–16 July 1986.
11. Wang, J.H.; Wan, D.C. Application progress of computational fluid dynamic techniques for complex viscous flows in ship and ocean engineering. *J. Mar. Sci. Appl.* **2020**, *19*, 1–16. [CrossRef]
12. Brizzolara, S.; Couty, N.; Hemundstad, O.; Kukkanen, T.; Ioan, A.; Viviani, M.; Temarel, P. Comparison of experimental and numerical loads on an impacting bow section. *Ships Offshore Struct.* **2008**, *3*, 305–324. [CrossRef]
13. Wang, S.; Guedes Soares, C. Stern slamming of a chemical tanker in irregular head waves. *Ocean Eng.* **2016**, *122*, 322–332. [CrossRef]
14. Xie, H.; Liu, F.; Yu, P.Y.; Ren, H.L. Numerical simulation on the water entry of bow-flare section considering bulbous bow. *Ocean Eng.* **2020**, *205*, 107081. [CrossRef]
15. Farsi, M.; Ghadimi, P. Simulation of 2D symmetry and asymmetry wedge water entry by smoothed particle hydrodynamics method. *J. Braz. Soc. Mech. Sci. Eng.* **2015**, *37*, 821–835. [CrossRef]
16. Wang, S.; Xiang, G.; Guedes Soares, C. Assessment of three-dimensional effects on slamming load predictions using OpenFoam. *Appl. Ocean Res.* **2021**, *112*, 102646. [CrossRef]
17. Wang, K.; Ma, X.; Bai, W.; Lin, Z.B.; Li, Y.B. Numerical simulation of water entry of a symmetric/asymmetric wedge into waves using OpenFOAM. *Ocean Eng.* **2021**, *227*, 108923. [CrossRef]
18. Bakica, A.; Malenica, S.; Vladimir, N. Hydro-structure coupling of CFD and FEM—Quasi-static approach. *Ocean Eng.* **2020**, *217*, 108118. [CrossRef]
19. Yu, P.Y.; Li, H.; Ong, M.C. Hydroelastic analysis on water entry of a constant-velocity wedge with stiffened panels. *Mar. Struct.* **2019**, *63*, 215–238. [CrossRef]
20. Luo, H.B.; Wang, H.; Guedes Soares, C. Numerical and experimental study of hydrodynamic impact and elastic response of one free-drop wedge with stiffened panels. *Ocean Eng.* **2012**, *40*, 1–14. [CrossRef]
21. Xie, H.; Ren, H.L.; Li, H.; Tao, K.D. Quantitative analysis of hydroelastic characters for one segment of hull structure entering into water. *Ocean Eng.* **2019**, *173*, 469–490. [CrossRef]
22. Lakshmynarayanana, P.A.; Temarel, P. Application of CFD and FEA coupling to predict dynamic behaviour of a flexible barge in regular head waves. *Mar. Struct.* **2019**, *65*, 308–325. [CrossRef]
23. Sun, T.; Zhou, L.; Yin, Z.; Zong, Z. Cavitation bubble dynamics and structural loads of high-speed water entry of a cylinder using fluid-structure interaction method. *Appl. Ocean Res.* **2020**, *101*, 102285. [CrossRef]
24. Shi, Y.; Pan, G.; Yim, S.C.; Yan, G.; Zhang, D. Numerical investigation of hydroelastic water-entry impact dynamics of AUVs. *J. Fluids Struct.* **2019**, *91*, 102760. [CrossRef]
25. Jiao, J.L.; Huang, S.X.; Tezdogan, T.; Terziev, M.; Guedes Soares, C. Slamming and green water loads on a ship sailing in regular waves predicted by a coupled CFD–FEA approach. *Ocean Eng.* **2021**, *241*, 110107. [CrossRef]
26. Liu, W.Q.; Luo, W.P.; Yang, M.; Xia, T.Y.; Huang, Y.; Wang, S.M.; Leng, J.; Li, Y. Development of a fully coupled numerical hydroelasto-plastic approach for offshore structure. *Ocean Eng.* **2022**, *258*, 111713. [CrossRef]
27. Yan, D.N.; Mikkola, T.; Kujala, P.; Hirdaris, S. Hydroelastic analysis of slamming induced impact on stiff and flexible structures by two-way CFD-FEA coupling. *Ships Offshore Struct.* **2022**, 1–3. Available online: https://www.tandfonline.com/doi/pdf/10.1080/17445302.2022.2116231?needAccess=true (accessed on 20 August 2022). [CrossRef]
28. Zhao, R.; Faltinsen, O.M.; Aarsnes, J.V. Water entry of arbitrary two-dimensional sections with and without flow separation. In Proceedings of the 21st Symposium on Naval Hydrodynamics, Washington, DC, USA, 19 August 1997; pp. 408–423.
29. De Backer, G.; Vantorre, M.; Beels, C.; De Pré, J.; Victor, S.; De Rouck, J.; Blommaert, C.; Van Paepegem, W. Experimental investigation of water impact on axisymmetric bodies. *Appl. Ocean Res.* **2009**, *31*, 143–156. [CrossRef]
30. Dong, C.R.; Sun, S.L.; Song, H.X.; Wang, Q. Numerical and experimental study on the impact between a free falling wedge and water. *Int. J. Nav. Arch. Ocean Eng.* **2019**, *11*, 233–243. [CrossRef]
31. Jiang, Y.C.; Bai, J.Y.; Dong, Y.; Sun, T.Z.; Sun, Z.; Liu, S.J. Investigations of air cushion effect on the slamming load acting on trimaran cross deck during water entry. *Ocean Eng.* **2022**, *251*, 111161. [CrossRef]
32. Jiao, J.L.; Huang, S.X.; Guedes Soares, C. Numerical investigation of ship motions in cross waves using CFD. *Ocean Eng.* **2021**, *223*, 108711. [CrossRef]
33. Deng, R.; Chen, S.Y.; Wu, T.C.; Luo, F.Q.; Jiang, D.P.; Li, Y.L. Investigation on the influence induced by interceptor on the viscous flow field of deep-Vee vessel. *Ocean Eng.* **2020**, *196*, 106735. [CrossRef]
34. Huang, S.X.; Jiao, J.L.; Guedes Soares, C. Uncertainty analyses on the CFD–FEA co-simulations of ship wave loads and whipping responses. *Mar. Struct.* **2022**, *82*, 103129. [CrossRef]
35. Wilson, R.V.; Carrica, P.M.; Stern, F. Unsteady RANS method for ship motions with application to roll for a surface combatant. *Comput. Fluids* **2006**, *35*, 501–524. [CrossRef]
36. ITTC. Recommended Procedures and Guidelines, 7.5-03-01-01, Uncertainty Analysis in CFD Verification and Validation Methodology and Procedures. 2017. Available online: https://www.ittc.info/media/8153/75-03-01-01.pdf (accessed on 20 August 2022).